

Benchmark Reynolds-averaged Navier-Stokes study of a generic marine rudder's static stall characteristics

Downloaded from: https://research.chalmers.se, 2025-10-17 06:15 UTC

Citation for the original published paper (version of record):

Bettle, M., Bordier, L., Slama, M. et al (2025). Benchmark Reynolds-averaged Navier-Stokes study of a generic marine rudder's static stall

characteristics. Ocean Engineering, 342. http://dx.doi.org/10.1016/j.oceaneng.2025.122847

N.B. When citing this work, cite the original published paper.

research.chalmers.se offers the possibility of retrieving research publications produced at Chalmers University of Technology. It covers all kind of research output: articles, dissertations, conference papers, reports etc. since 2004. research.chalmers.se is administrated and maintained by Chalmers Library

ELSEVIER

Contents lists available at ScienceDirect

Ocean Engineering

journal homepage: www.elsevier.com/locate/oceaneng



Research paper

Benchmark Reynolds-averaged Navier-Stokes study of a generic marine rudder's static stall characteristics

Mark Bettle^{a,*}, Luc Bordier^b, Myriam Slama^b, Emmanuel François^b, Serge Toxopeus^c, Craig Marshall^d, Richard Pattenden^e, Riccardo Broglia^f, Shawn Aram^g, Abel Vargas^g, Rui Lopes^h, Magnus Vartdal^j, Tom Keith^j, Carl Janmark^k, Tiger Jeans^d, Andrew Gerber^d, Rickard Bensow^h, Toby Peacock^l

- ^a Defence Research and Development Canada (DRDC), Canada
- ^b SIREHNA / Naval Group, France
- ^c Maritime Research Institute Netherlands (MARIN), The Netherlands
- d University of New Brunswick (UNB), Canada
- e QinetiQ, United Kingdom
- f CNR-INM, Italy
- g Naval Surface Warfare Center Carderock Division (NSWCCD), United States
- h Chalmers University of Technology, Sweden
- i FFI. Norway
- ^j Defence Science and Technology Group (DSTG), Australia
- k FOI. Sweden
- ¹BAE Systems, United Kingdom

ARTICLE INFO

Keywords: RANS Rudder Stall Hysteresis Verification Benchmark Submarine

ABSTRACT

When assessing manoeuvring performance it is common to perform steady Reynolds-Averaged Navier-Stokes computations for a range of turning conditions. It is then critical to reliably and accurately predict rudder forces. A recent collaborative benchmark study showed inconsistent capturing of stall effects on aft control surfaces for a generic submarine. To investigate this issue, we present a new generic marine rudder and the influence of the numerical setup on the prediction of its static stall characteristics. We demonstrate the existence of a static hysteresis loop, which we compute with Menter's $k-\omega$ SST turbulence model at a full-scale Reynolds number of 7.44×10^6 . One branch shows a light trailing-edge stall with a high lift coefficient, and the other a deep stall with a low lift coefficient. We show how the initial conditions and solution methodology affect which solution is achieved. Notably, even 1° below the low limit in the hysteresis loop, an incorrect deep-stall result can be obtained when using a free-stream initialization, due to poor iterative convergence. In contrast, potential-flow initialization and unsteady RANS methods effectively produce the correct high-lift solution below the hysteresis loop. A discretization analysis at $\alpha=24^\circ$ shows that six flow solvers produce consistent results to within a small discretization uncertainty.

1. Introduction

Manoeuvring behaviour is a critical component in the development of new ship concepts. The starting point when assessing manoeuvring characteristics is often models based on a quasi-steady assumption, such as that of Gertler and Hagen (1967) which is commonly used in the submarine community (Renilson, 2018). Then, the hydrodynamic forces and moments on a submarine are calculated by constant coefficients multiplied by the vehicle's instantaneous velocity and acceleration state.

Static experiments or computations are typically used to generate coefficients and unsteady effects are accounted for with added mass coefficients, which do not account for the motion history. During the early design phase as well as to account for ship scale performance, computational fluid dynamics (CFD) has become a practical tool for predicting marine vehicle hydrodynamics. As the bulk of the computations will be for steady conditions, computationally-efficient Reynolds-Averaged Navier-Stokes (RANS) methods form the industry standard, and are the only available option for ship scale assessment. Chen and Yao (2024)

E-mail address: mark.bettle@ecn.forces.gc.ca (M. Bettle).

^{*} Corresponding author.

recently demonstrated the process of evaluating Gertler and Hagen manoeuvring coefficients for the SUBOFF submarine using RANS computations of steady captive motions. It is important to note that approximately 400 individual RANS computations were required in this study and not all Gertler and Hagen coefficients were evaluated (such as those for control surface deflections). The large number of required computations emphasizes the necessity for computationally-efficient methods for this application. Yao et al. (2021) demonstrated a similar approach of using RANS computations to evaluate manoeuvring derivatives for fast-time free-running manoeuvring simulations of a surface ship.

A recent NATO Applied Vehicle Technology (AVT) collaboration on the flowfield prediction for manoeuvring underwater vehicles (AVT-301) used the BB2 generic submarine geometry to benchmark and validate CFD methods for predicting both the hydrodynamic loads and flowfields for underwater vehicles (NATO AVT-301 Task Group, 2022; Toxopeus et al., 2022). The BB2 geometry was defined jointly by the Maritime Research Institute Netherlands (MARIN) and Defence Science and Technology Group (DSTG) to enable collaborative hydrodynamic studies of underwater vehicles, including the assessment of CFD methods. It is a variant of the Joubert concept submarine (Joubert, 2006), which incorporates modifications for improved stability and control characteristics, such as enlarged tailplanes (Bettle, 2014; Overpelt et al., 2015). Several physical models of the BB2 submarine have been built for hydrodynamics experiments, including MARIN's free-running model (Overpelt et al., 2015), DSTG wind tunnel models (Lee et al., 2023, 2024), and a towing tank model (Kim et al., 2023). In the large AVT-301 collaboration, participants performed CFD computations of steady captive BB2 motions that are typically used for manoeuvring coefficient evaluation. A good general agreement was obtained between RANSbased predictions and DSTG wind tunnel experiments for the mean flow field and overall hydrodynamic loads for the BB2 at drift angles of 0 and 10 degrees. However, inconsistent results were obtained for different RANS predictions of the hydrodynamic loads on the submarine undergoing steady rotation. There was large scatter even when only considering results for Menter's $k-\omega$ Shear Stress Turbulence model (SST) (Menter, 1994; Menter et al., 2003), which is a popular model for marine vehicle applications. Rotating arm experiments conducted by QinetiQ (Thompson, 2017) were provided to the AVT-301 group for comparison of overall hydrodynamic forces and moments for several drift angles and rotation rates. While some CFD simulations agreed better than others with the experiments, none agreed satisfactorily for all force and moment components and all conditions. A breakdown in CFD hydrodynamic loads by component (hull, sail, sail planes, aft control surfaces) showed that the scatter was due to differences in force predictions for the aft control surfaces (ACS). An analysis of the CFD flow field showed that this was a result of some computations predicting stall for two of the ACSs while others predicted stall for one of them or neither of them. Since only the total vehicle hydrodynamic forces and moments were measured in the experiments, it could not be determined conclusively which ACSs were stalled (if any) in the experiments. Rudder stall was not an issue in the wind tunnel validation case because the steady 10° drift angle was well below the stall angle, whereas in the rotatingarm cases, the local drift angle at the aft control surfaces ranged up to approximately 22°.

The primary objective of this paper is to examine the inconsistencies in the AVT-301 RANS predictions of submarine ACS flows at high incidence through a detailed solution verification study (see (Eça et al., 2010) for a description of solution verification), aiming to enable more reliable and repeatable RANS-based predictions for applications such as manoeuvring coefficient evaluation. It can be argued that RANS is not suitable for studying stall behaviour but that one should use scale-resolving methods. In particular, the statistically unsteady flow of a separated stall flow condition cannot be meaningfully represented by steady RANS. The aim of this paper is not to accurately compute the stalled flow condition with RANS. Our focus is on achieving consistent and reliable force and moment predictions for a given RANS model up

to the point of stall. This includes consistent and repeatable predictions of the critical angle of attack at which stall occurs. The pre-stall data is generally what is required for manoeuvring coefficient evaluation for traditional manoeuvring models, which were not designed to capture the sudden changes in forces and moments that occur during stall. A recent review of CFD methods for underwater vehicles by He et al. (2024) shows that Large Eddy Simulation (LES) has become an indispensable tool for understanding details in the flow. It is particularly useful for cases where resolving turbulence is critical, such as hydroacoustic applications (Rocca et al., 2022). However, LES is not yet widely used due to computational expense, which increases significantly with Reynolds number. Liefvendahl and Fureby (2017) estimate that 4.9×10^{12} grid cells are needed to perform wall-resolved LES computations for a conventional submarine at full-scale conditions, which is well beyond the capacity of computers today. In contrast, wall-modelled LES (WMLES) is estimated to require approximately 2.5×10^9 cells, a size that is now feasible for computing a limited number of conditions but is too expensive for exploring the large solution spaces required for the generation of hydrodynamic coefficients for a manoeuvring model. There is also increased interest in hybrid RANS-LES methods that solve the RANS equations near wall boundaries to reduce computational expense while resolving most of the turbulent length scales elsewhere with LES. This would relax the grid cell count further but the need for transient simulations still makes this infeasible. Due to the relatively low expense of RANS methods at full scale, they are expected to continue being a central tool for practical marine vehicle hydrodynamics analyses for many years to come, particularly for manoeuvring applications where the desired output is the integrated hydrodynamic forces and moments.

Further, a primary focus to-date has been on model-scale computations due to the widespread availability of high-quality benchmark and validation data, but there is increasing interest in simulating fullscale conditions (Terziev et al., 2022). A recent full-scale validation study of the delivered power for a 180-meter long cargo vessel, (Orych et al., 2021), showed a very close agreement, with a comparison error of around 1%, between sea trials and RANS simulations with an explicit algebraic stress turbulence model and wall roughness modelling. An important component of this study was the use of systematic grid refinement to estimate numerical uncertainty, which was reduced to 1.4%. The study was extended to 14 different vessels by Korkmaz et al. (2023) with similar good agreement. Pereira et al. (2017) performed a literature survey of RANS computations for the KRISO Very Large Crude Carrier 2 (KVLCC2), for which they found 160 results at model scale (Reynolds number based on length of $Re_L = 4.6 \times 10^6$) and full scale $(Re_L = 2.03 \times 10^9)$. They found significant scatter in predictions of the resistance coefficient, particularly for results based on grids with less than 10⁶ cells, in which case the comparison error with experiments ranged up to 70%. They then performed a thorough numerical uncertainty study with 14 RANS turbulence models at model scale and four models at full scale, which showed that the turbulence model can have a significant effect on integrated forces as well as flow fields. Recently, several joint workshops have been performed within the JoRes project¹ for powering predictions and by Chalmers for pure resistance (Lopes et al., 2025). These studies highlight the potential for RANS to provide accurate predictions of ship hydrodynamics while also emphasizing the requirement for careful verification and validation studies for obtaining reliable predictions. We remark that all studies in full-scale have been performed for steady straight ahead conditions.

To work towards manoeuvring assessment in full-scale, the NATO AVT-392 working group was formed in 2023 as a follow-on to AVT-301 to assess numerical predictions of flow around marine rudders, with a focus on large angles of attack around the stall point in both model and full-scale. While there have been several studies done on high aspectratio wings and 2D airfoils for aerodynamics applications, there are

¹ https://www.jores.net

relatively few studies in the open literature on low-aspect ratio wings, which are more directly relevant to marine vehicles. One of the largest studies was done by Whicker and Fehlner (Whicker and Fehlner, 1958), which considered effective aspect ratios in the range of 1 to 3 at Reynolds numbers based on chord from 10^6 to 3×10^6 . These experiments provided a valuable dataset that continues to be used for empirical predictions of hydrodynamic forces and moments for marine vehicles (Molland and Turnock, 2022). However, this dataset did not contain flow field measurements, which are important for more comprehensive validation of numerical predictions and physical insight on stall phenomenon. It is also hypothesized that the large discrepancies observed in the CFD predictions for AVT-301 may be related to flow hysteresis, which was not studied in the Whicker and Fehlner experiments. To fill the gap in desired experimental validation data, the AVT-392 group has defined a new generic rudder geometry. It is designed to be used for wind tunnel experiments in which a floor (or wall) mounting gives an overall flow condition that is relevant for submarine ACSs, using the BB2 as a guide for this. However, the new rudder's overall characteristics - low aspect ratio, taper, and NACA0016 profile - make it relevant as a general benchmark geometry for numerical studies of marine vehicle control surfaces. In this paper, we present this geometry for the first time and use it to benchmark RANS-based predictions of its static stall.

Other studies have highlighted the challenges of predicting stall using RANS models. Kamenetskiy et al. (2014) present evidence for the existence of multiple RANS solutions with the Spalart-Allmaras (SA) and Wilcox two-equation $k - \omega$ turbulence models. This was demonstrated with the NACA0012 airfoil and a high-lift trap wing configuration, at large angles-of-attack around the stall point. For coarse-grid computations of the trap wing at an angle of attack of 28°, eight distinct solutions were obtained with the SA model and three were obtained with the Wilcox model. All solutions were converged to machine accuracy. A grid refinement study was conducted with the SA model and the number of solutions was reduced to two for the finest grid, indicating that some coarse-grid results might be spurious numerical artifacts rather than solutions to the continuous partial differential equations. The occurrence of multiple solutions was attributed to smooth body separation, an aspect of many flows of practical interest. The authors emphasize that the CFD community should be aware of this phenomenon of multiple solutions and should place greater emphasis on obtaining reliable, converged solutions. It should also be noted that several turbulence closures have been demonstrated to have non-unique solutions (Rumsey, 2007) and the interaction of such model properties with stalled flow regions is likely to be problematic.

In some cases, two flow solutions can arise due to flow hysteresis. This is a phenomenon whereby fully attached and massively separated flow can be observed at the same angles of attack, depending on whether the angle of attack is increasing or decreasing. This phenomenon has been observed experimentally for several airfoils (Broeren and Bragg, 2001; Hristov and Ansell, 2018) and for a NACA0020 rudder with an aspect ratio of 2 in the recent work by Simonet et al. (2024). Richez et al. (2016), Busquet et al. (2021), and Sereez et al. (2024) have also studied airfoil and wing hysteresis and bifurcation behaviour numerically. Hysteresis is typically studied under quasi-static conditions where the rate of change of the angle of attack is small enough to not play a dynamically important role. Interestingly, it has been observed both experimentally (Zaman et al., 1989) and numerically (ElAwad and ElJack, 2019) that close to stall the lift undergoes low frequency oscillations with a Strouhal number on the order of 10⁻², which is an order of magnitude less than those observed for bluff body separation. In 2D simulations, Busquet et al. (2021) observed instabilities with Strouhal numbers on the order of 10^{-3} for the OA209 foil close to stall. However, Sarras and Marquet (2024) later demonstrated for the NACA0012 that the most unstable mode close to stall is threedimensional, and a pure two-dimensional mode is therefore unlikely to be important in practice. To comply with the quasi-static condition, the rate of angle of attack adjustment may need to be significantly slower

than the time scale of the low frequency flow oscillation close to stall. Le Fouest et al. (2021) performed experiments with a NACA0018 blade and found that it takes on the order of 50 convective times for the stall process to complete when rotating slowly past the critical angle. This includes a reaction delay of 32 convective times during which the critical stall angle is exceeded but there is little change in lift. They recommend that "conventional measurements of the static stall angle and the static load curves should be conducted using a continuous and uniform rampup motion at a reduced frequency around 1×10^{-4} " (Le Fouest et al., 2021). Given this strict time scale restriction it is likely that manoeuvres in a practical setting will involve non-negligible dynamic effects, and the static stall predictions should be supplemented by information regarding the rudder dynamic stall. The present work is confined to static and quasi-static conditions, i.e., for fixed and slowly changing angles of attack. We plan to evaluate dynamic effects in a follow-on study.

This paper is structured as follows. We first describe the development of the AVT-392 rudder in Section 2 and define the flow and boundary conditions for a collaborative numerical benchmark in Section 3. In Section 4, we describe our approach to solving this benchmark with the aim of investigating the inconsistencies in RANS predictions of control surface stall observed in AVT-301. The study is conducted in two phases for this purpose: in the first, each participant performs computations independently with their best practices for meshing and solution procedure, similar to those used for the AVT-301 study with the BB2. The purpose of this phase is to see if the scatter in stall predictions observed for the BB2 ACS during steady turning is reproduced with the new isolated rudder geometry. In the second phase, a common set of grids and the SST turbulence model are used to perform a discretization uncertainty analysis and explore the effect of initialization and solution strategy. The same turbulence model and grid set are then used to identify a static hysteresis loop. The two stages were done at Reynolds numbers based on mean chord of $Re_c = 1 \times 10^6$ and $Re_c = 7.44 \times 10^6$, except the hysteresis loop was only investigated at $Re_c = 7.44 \times 10^6$. The trends were consistent for both conditions so this paper will mainly focus on the higher Reynolds number, which is representative of a full-scale condition. Our results, which include a comprehensive discretization uncertainty analysis comparing six flow solvers and six geometrically-similar grids, are presented in Section 5. The paper ends with a summary of key findings and recommendations in Section 6.

2. Rudder geometry definition

The new benchmark rudder geometry defined for this work is derived from the BB2 ACS, which are shown in Fig. 1. These ACS are based on a NACA0016 profile. Some modifications were made to adapt this geometry for planned wind tunnel testing, where the root of the rudder is to be mounted on a flat tunnel floor instead of the curved BB2 tail cone. RANS computations of the BB2 undergoing straight-and-level flight (zero flow incidence with respect to the hull axis) were run to determine the relative flow incidence angles at the ACS's tips and leading and trailing edges. The commercial flow solver Ansys CFX and the 2003 version of Menter's $k-\omega$ SST model (Menter et al., 2003) were used for these computations. A half-body hybrid mesh with 51×10^6 cells on the starboard



Fig. 1. Photo of MARIN's free-running BB2 model.

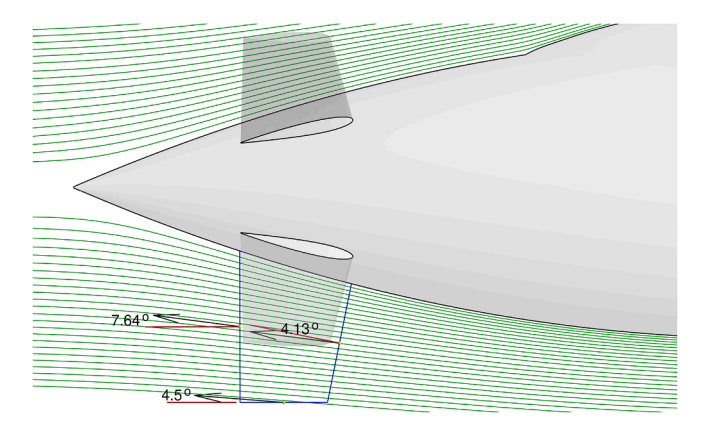


Fig. 2. RANS prediction of symmetry-plane streamlines (green) around the stern of the BB2 (grey) for $Re_L = 250 \times 10^6$. The blue lines show the rotational projection (about the hull axis) of the aft control surface planform onto the symmetry plane. Velocity vectors are shown at the midpoints of the leading edge (LE), trailing edge (TE), and tip of the projected planform. The angles displayed are with respect to projected LE and TE normal vectors and the planform tip tangent vector (red lines).

side of the BB2's plane of symmetry was used, which was previously developed and tested by Defence Research and Development Canada (DRDC) - see mesh 'Grd22-Sf-L5' in Bettle (2020) for complete mesh details. These computations were run at a Reynolds number based on submarine length of $Re_L=250\times10^6$, which corresponds to a full-scale BB2 speed of approximately 8 knots in 15°C seawater. For this condition, the average first-node y^+ over the BB2 surface was 0.75. Fig. 2 shows the computed streamlines around the stern of the BB2 on the symmetry plane. The planform outline of one ACS was rotated about the hull axis to the symmetry plane under the BB2 hull, as shown by the blue outline in Fig. 2. This shows the relative angle between the leading edge, trailing edge, and tip with respect to the flow around the hull at the axial position of the aft control surfaces. The streamlines are tangent to the hull at the root of the ACS, but they become noticeably more aligned with the free-stream at the ACS tip.

Since it is not possible to replicate the diverging, curved streamlines around the hull in the planned wind tunnel experiments, it was decided to approximately match the relative flow incidence at the midpoints of the leading edge, trailing edge, and tip, for zero rudder deflection. These flow incidence angles, shown in Fig. 2, were calculated to be 4.13°, 7.64°, and 4.5°, respectively. These angles were rounded and used to set the leading edge sweep ($\beta_L \approx 4^\circ$), trailing edge sweep ($\beta_T \approx 8^\circ$), and the tip inclination angle ($\gamma \approx 4.5^{\circ}$) for the AVT-392 benchmark geometry, as shown in Fig. 3. The AVT-392 rudder is constructed with NACA0016 profiles that are parallel to the root chord. Like the BB2 rudders, the trailing edge is truncated using a 15 mm fillet at full scale, which shortens the chord by $\approx 1\%$ (the precise truncation percentage varies with span due to taper), as shown in Fig. 4. An approximate mean chord, \bar{c} , is used for the reference chord. It is defined to be the chord of the underlying NACA0016 profile (prior to rounding/truncation) at the leading edge mid-span, $s_{LE}/2$, as shown in Fig. 3. This is only an approximation to the mean chord as it neglects the small slanted tip region above the leading edge span in addition to the trailing edge truncation/rounding. The rotation axis for the AVT-392 rudder is normal to the root chord and passes through the quarter-chord of the NACA0016 profile at $s_{LE}/2$. The reference planform area for the AVT-392 rudder, A_p , is approximated by the area enclosed by the underlying untruncated NACA0016 planform, shown in red in Fig. 3. It includes the slanted tip region but does not account for the trailing edge rounding or the slightly-domed tip. These choices for reference parameters were done because they are defined exactly, they approximate the true geometry with only a small error (less than 1% for planform area and order of 1% for mean chord), and

Table 1Geometric parameters for the AVT-392 rudder.

Symbol [unit]	Parameter	Full Scale	Model Scale (NRC)
λ b [m] c _r [m]	Scaling Ratio Total span (root to tip) Root chord	1 4.2273 3.6058	1:1.428571 (0.7:1) 2.9591 2.5240
$\begin{array}{l} s_{LE} \ [m] \\ \bar{l} \ [m] \\ A_p \ [m^2] \\ \beta_L \ [^\circ] \\ \beta_T \ [^\circ] \\ \gamma \ [^\circ] \end{array}$	Leading edge span Reference chord Reference area Leading edge sweep Trailing edge sweep Tip inclination		2.800 2.254 6.46212 0) $\approx 4.00^{\circ}$ (4220) $\approx 7.97^{\circ}$ 769.2) $\approx 4.54^{\circ}$

Table 2Specified flow properties.

Quantity	Value(s)
Free stream velocity, U_{∞}	50 m/s, 6.725 m/s
Air density, ρ	1.204 kg/m ³
Air viscosity, μ	$1.825 \times 10^{-5} \ Pa-s$
$Re_c = \rho U_{\infty} \overline{c} / \mu$	7.435×10^6 , 1.0×10^6

it is anticipated that some comparison studies may be made in the future that look at variations in the tip and trailing edge details, while retaining the underlying NACA0016 profiles. A summary of the overall dimensions for the AVT-392 rudder are given in Table 1, for full scale and a 70% model scale selected for wind tunnel experiments that are being planned at the National Research Council of Canada's (NRC) 9meter low-speed wind tunnel in Ottawa, Canada. Here, the total span, b, and root chord, c_r , are for the actual AVT-392 rudder geometry with trailing edge rounding and domed tip (the slightly different values for the underlying NACA0016 are shown in Fig. 3). Note that the original BB2 rudders are split part way along the span into a hull-fixed portion and a rotating portion (see Fig. 1) whereas the AVT-392 geometry is defined as an all-moving rudder. For comparison with other finite wing geometries, the AVT-392 rudder's untruncated NACA0016 base planform without the slanted tip has an aspect ratio of $s_{LE}/\bar{c} \approx 1.24$ and a taper ratio of $c_t/c_r = 2800/3640 \approx 0.77$.

3. Benchmark Problem Definition

3.1. Domain and boundary conditions

The flow and boundary conditions are set for this benchmark CFD study to approximately match those expected for the planned experiments at NRC's 9-meter tunnel. A 70% geometric scale is selected for the physical model, giving a span (from floor to tip) of b = 2.9591 m and a reference chord of $\overline{c} = 2.254$ m, as indicated in Table 1. At this scale, the blockage ratio of the rudder in the tunnel is approximately 4.4% for a rudder deflection of 35°. The rudder geometry is placed in the simplified tunnel domain shown in Fig. 5. The root of the rudder is placed on the tunnel floor. A uniform-flow inlet boundary is placed 21 m upstream of the rudder's rotation axis to develop a boundary layer thickness that is consistent with that estimated for the empty NRC wind tunnel at that location (approximately 7% of the root-to-tip span at $Re_c = 7.44 \times 10^6$). Two velocities are specified for the inlet: 50 m/s to match the anticipated maximum speed for the NRC tunnel tests and 6.725 m/s to give a Reynolds number of $Re_c = 10^6$. A pressure outlet boundary is placed $\approx 22.6\overline{c}$ downstream of the rudder axis, where the reference pressure is set to zero. The floor and rudder boundaries are given a no-slip boundary condition while the sides and top boundaries of the tunnel are given free-slip (zero wall shear stress) boundary conditions. Several anglesof-attack, α , are simulated by rotating the rudder about the negative z-axis, as indicated by the coordinate system in Fig. 5, to determine the static stall angle. By this convention, positive α gives positive lift. The specified flow properties and boundary conditions are summarized in Table 2 and Table 3, respectively.

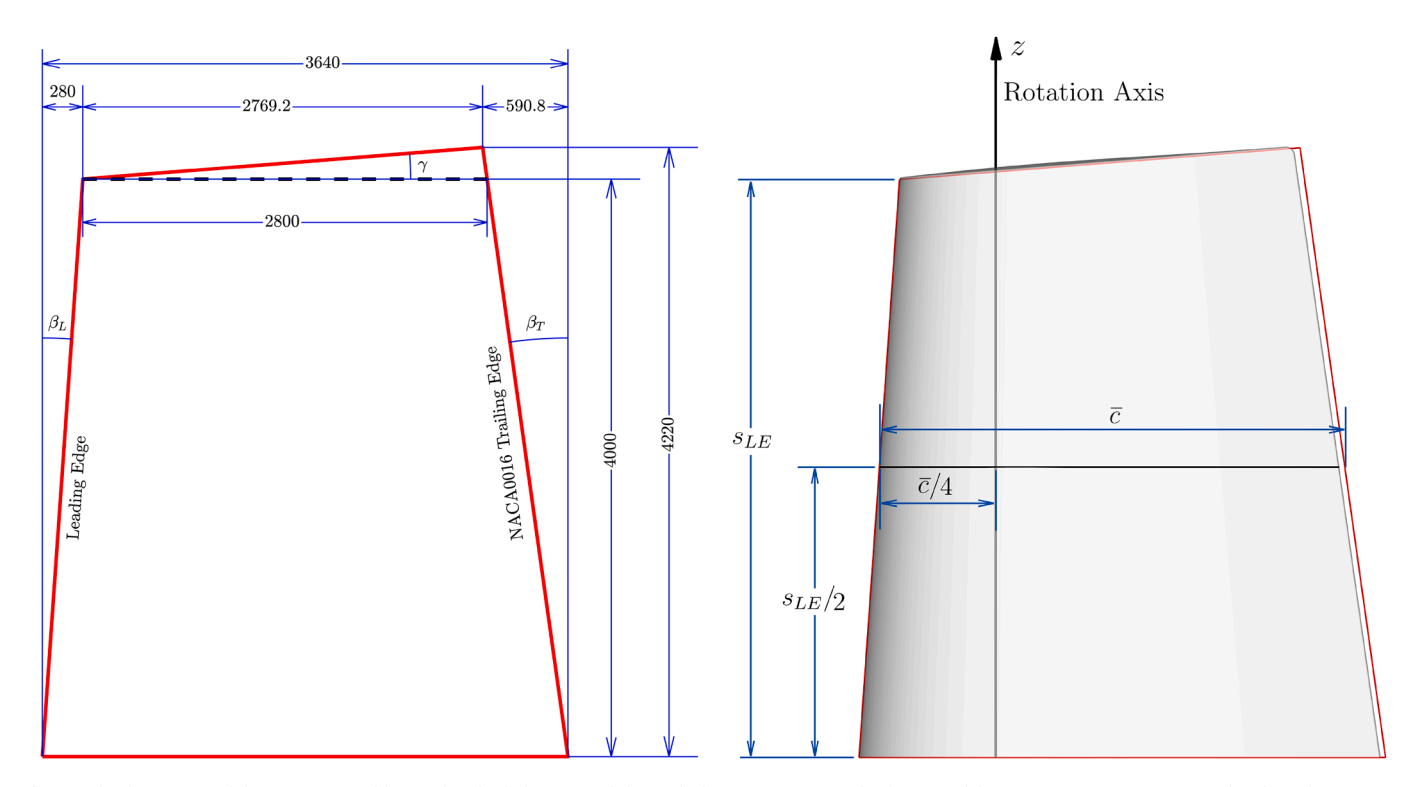


Fig. 3. Planform view of the AVT-392 rudder (right, shaded grey) and the underlying NACA0016 planform used for geometry construction (red). The reference area A_p is taken to be the area bounded by the red lines. Dimensions are given in millimetres at full scale.

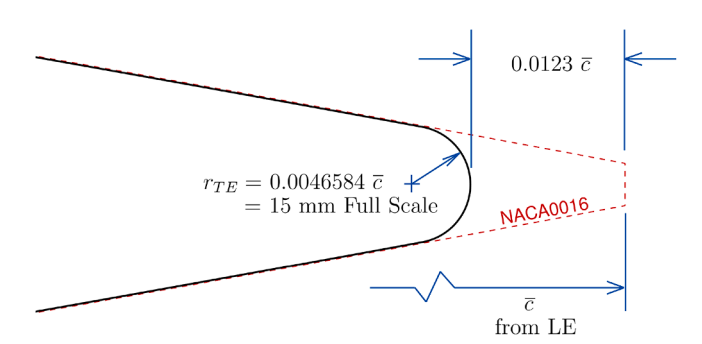


Fig. 4. AVT-392 rudder trailing-edge rounding at the leading edge mid-span, $s_{LE}/2$, relative to the underlying NACA0016 profile (red dashed lines) used for geometry construction.

Table 3 Specified boundary conditions.

Boundary	Boundary Condition
Inlet	Velocity in the x-direction set to U_{∞} , velocity in y- and z-directions set to zero, turbulent intensity set to 1%,
	and eddy viscosity ratio (μ/μ_t) set to 1.
Outlet	Pressure (or average pressure) set to 0.
Rudder	Smooth, no-slip wall
Tunnel floor	Smooth, no-slip wall
Tunnel sides and top	Free-slip wall (wall shear stress set to zero)

3.2. Data normalization

The lift, L, drag, D, yawing moment about the rudder's rotation axis, M_z , pressure, P, and wall shear stress components, τ_x , τ_y , τ_z , are made non-dimensional as follows:

$$C_L, C_D = \frac{L, D}{0.5 \rho U_\infty^2 A_p},\tag{1}$$

$$C_{Mz} = \frac{M_z}{0.5\rho U_\infty^2 A_p \overline{c}},\tag{2}$$

$$c_{p}, \tau'_{x}, \tau'_{y}, \tau'_{z} = \frac{P, \tau_{x}, \tau_{y}, \tau_{z}}{0.5 \rho U_{\infty}^{2}}.$$
(3)

Vortex structures are visualized using iso-surfaces of the Q-criterion, Q, as proposed by Hunt et al. (1998), which is normalized as follows:

$$Q' = Q\left(\frac{\overline{c}}{U_{\infty}}\right)^2,\tag{4}$$

where Q is the second invariant of the velocity gradient tensor, ∇u . The helicity, $H = \mathbf{u} \cdot \boldsymbol{\omega}$, is used to show the sense of rotation of vortices and it is made non-dimensional as follows:

$$H' = \frac{H}{|\boldsymbol{\omega}| \cdot |\mathbf{u}|},\tag{5}$$

where ω and \mathbf{u} are the vorticity and velocity vectors, respectively.

4. Methodology

This collaborative study, involving a total of ten organizations and six flow solvers, is divided into two phases. In the first phase, participants perform computations using their own grids and solver methods independently of each other. The purpose of these initial computations is to see if the scatter observed in AVT-301 for the BB2 is reproduced with the newly-defined rudder on a plane boundary in place of the hull form. In the second phase, a common set of grids and Menter's $k-\omega$ SST turbulence model are used by all participants to more directly compare the effects of different CFD solvers and solver settings. Incompressible flow solvers with second-order accurate spatial discretization schemes and double-precision numerics are used for both phases. Descriptions of the SST turbulence model and all flow solvers are given in Subsections 4.1 and 4.2. This is followed by a summary of Phase 1 and Phase 2 computations, respectively.

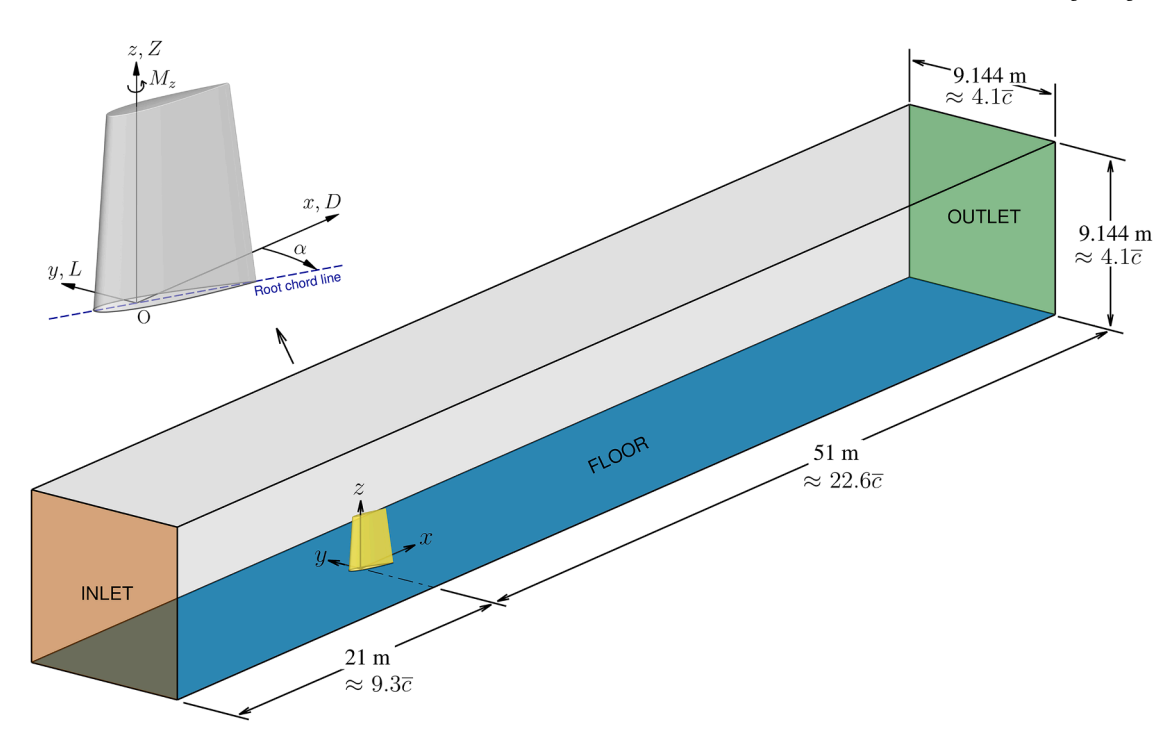


Fig. 5. Computational domain and coordinate system used for the benchmark CFD study, $\bar{c} = 2.254$ m.

4.1. SST turbulence model

The focus of this study is on the $k-\omega$ SST turbulence model proposed by Menter (1994). This two-equation eddy viscosity model solves a $k-\omega$ model near solid, no-slip boundaries, where k is turbulent kinetic energy and ω is the specific dissipation rate. This enables grids to be resolved into the viscous sublayer without the use of damping functions required in $k-\varepsilon$ formulations (where ε is turbulent dissipation). Away from solid boundaries and out to the far-field, it switches to a $k-\varepsilon$ model using a blending function. This avoids the strong sensitivity to free-stream turbulence level observed for the $k-\omega$ model. This blending is also present in Menter's baseline (BSL) $k-\omega$ turbulence model (Menter, 1994). The SST model addresses the over-prediction of eddy viscosity, μ_t , in the BSL model by modifying the formulation for μ_t to account for the transport of turbulent shear stress. This improves the prediction for the onset and amount of flow separation from smooth surfaces (Menter, 1994), an important characteristic for the present study.

As documented on the NASA Langley Research Center Turbulence Modeling Resource Website (NASA Langley Research Center, 2025), there are several variations of the SST model. The original model described in the 1994 publication (Menter, 1994) will be referred to here as SST-1994. Several minor updates were made in a revision described by Menter et al. (2003). This version will be referred to as SST-2003. The primary change was the use of the strain invariant rather than magnitude of vorticity in the definition of eddy viscosity, but there was also a change in production limiters and minor changes to a couple of coefficients. For some solvers, there is a mixture of versions or the precise formulation is not known – for these non-standard variants, we use the designation "SST-ns".

It should be noted that the SST model is sensitive to grid resolution, but the solution is unique for a given combination of grid and numerical method (Rumsey, 2007), and the bifurcation of the solutions near stall should therefore not be a result of a pure turbulence model bifurcation.

4.2. CFD solvers

4.2.1. Ansys CFX

Ansys CFX is a multi-purpose commercial CFD software which uses a node-centred finite-volume method. All solution variables are co-located

at the mesh nodes and control volumes for the conservation equations are constructed around each node using the median-dual scheme. Finite-element shape functions are used to interpolate quantities to the integration points on the control volume surfaces for the evaluation of surface fluxes. In order to avoid a decoupled/checkerboard pressure field, the discretization of mass flows through control volume surfaces is based on the method of Rhie and Chow (1983), which was modified by Majumdar (1988). Ansys CFX uses a coupled solver in which the discretized mass and momentum equations are solved together as one system of equations. The steady-state CFX solver uses a pseudo timestep for iterative convergence. At each pseudo timestep, the linearized equations are solved using an additive correction algebraic multigrid method.

DRDC and the University of New Brunswick (UNB) used version 2022R2 of Ansys CFX for this study. UNB used the steady-state solver for Phase 1. DRDC used the steady solver for Phase 1, and both the steady and unsteady solvers for Phase 2. DRDC also used a cylindrical rotating domain and sliding interface to perform unsteady RANS (URANS) computations of the rudder rotating at a slow constant rate in Phase 2. All DRDC URANS computations are done using second order temporal discretization.

4.2.2. Ansys Fluent

Ansys Fluent is a multi-purpose commercial CFD software with a variety of physical modelling capabilities, including multi-phase and discrete phase models, conjugate heat transfer, chemical reactions, and acoustics among others. The code uses a cell-centred finite volume method to solve the conservation equations on unstructured grids. Ansys Fluent defaults to using a least squares gradient reconstruction to compute the control volume surface fluxes, but also has Gauss Green cellbased and Gauss Green node-based methods. Like Ansys CFX, the Rhie and Chow (1983) method is used to avoid non-physical pressure distributions with the collocated velocity and pressure fields. Several SIMPLElike segregated solution algorithms are available, as well as a coupled algorithm with the capability of running on GPU-based architectures. The linearized equations are solved with an additive correction based algebraic multigrid method. Finally, like the other commercial solvers, Fluent contains turbulence models for all relevant industry standard methods (i.e. RANS, Detached-Eddy Simulation (DES), LES), and can be run with either steady-state or transient schemes.

DSTG used Version 2021R1 of Ansys Fluent for Phase 1 computations, using the steady-state solver and Gauss Green node-based method. *UNB* used Version 2024R2 for Phase 2, using the unsteady solver and the least square gradient construction for surface fluxes.

4.2.3. REFRESCO

REFRESCO (Vaz et al., 2009) is MARIN's in-house CFD solver, which is based on a finite volume discretization of the continuity and momentum equations written in strong conservation form. The solver uses a fully-collocated arrangement and a face-based approach that enables the use of cells with an arbitrary number of faces. Picard linearisation is applied and segregated or coupled approaches are available with mass conservation ensured using a SIMPLE-like algorithm (Klaij and Vuik, 2013) and a pressure-weighted interpolation technique to avoid spurious oscillations (Miller and Schmidt, 1988). Several alternative mathematical formulations can be used to solve turbulent flow. Thorough code verification is performed for all releases of REFRESCO (Eça et al., 2016).

MARIN used Version 2023.9 of REFRESCO for Phase 1 and Version 2024.1 for Phase 2, in all cases using the segregated solver. To compute the flow at several angles of attack in Phase 2, MARIN used grid deformation of the conformal DRDC grid within REFRESCO.

4.2.4. STAR-CCM+

STAR-CCM+ is a generic multi-purpose commercial flow solver originally developed and distributed by CD-Adapco, and now part of Siemens PLM Software engineering suite. This is a finite-volume-based solver running with unstructured meshes composed of arbitrary shaped cells (hexahedra dominant or polyhedra). It provides a range of models for turbulence, as well as many other capabilities relevant to marine applications such as multiphase flows and mesh motions. Steady-state RANS approaches and unsteady LES and DES are available. Steady or unsteady flows can be resolved by means of a coupled solver or a segregated solver using predictor / corrector algorithm to couple pressure and velocity (SIMPLE-like algorithm). It uses co-located variables with a Rhie-Chow type pressure-velocity coupling. Note that the SST turbulence model in STAR-CCM+ is based on the 1994 model coefficients but the modulus of the strain rate tensor is used instead of the vorticity tensor, and so it can not be categorized as either the 1994 or 2003 version. Also, by default, the STAR-CCM + does not use the 1994 or 2003 production limiter. There is no limiter enforced on the production of *k*; instead, there is an additional limiter on the turbulent viscosity based on Durbin's realizability constraint.

<code>QinetiQ</code> used STAR-CCM + version v16.06 for Phase 1 and v2210 for Phase 2. <code>Naval Group</code> (NG) used v2210 for both phases, and Chalmers University of Technology (<code>Chalmers</code>) used v2310 for Phase 2. The segregated solver with the SIMPLE-like algorithm was the approach employed by all institutes using STAR-CCM + .

4.2.5. OpenFOAM

The open-source CFD toolkit OpenFOAM (https://openfoam.com/) provides a large set of solvers for a multitude of flow problems, ranging from incompressible single-phase problems to multiphase flows with mass transfer, combustion, and compressibility. The spatial discretization is performed using a cell-centred co-located FV method for unstructured meshes with arbitrary cell-shapes, and a multistep scheme is used for the time derivatives. To complete the FV-discretization the face fluxes need to be reconstructed from grid variables at adjacent cells, requiring interpolation of the convective fluxes and difference approximations for the inner derivatives of the diffusive fluxes; see Weller et al. (1998) for more details on the discretization and the numerics used in OpenFOAM.

For this study, The Swedish Defence Research Agency (FOI) used OpenFOAM v2212 with the simpleFoam application for Phase 1 computations. The Institute of Marine Engineering within Italy's National

Research Council (CNR-INM) used OpenFOAM v2306 for Phase 2, also here with simpleFoam.

4.2.6. NavyFOAM

NavyFOAM (Kim et al., 2017) is an integrated Computational Fluid Dynamics package based on OpenFOAM (Weller et al., 1998), developed at the Naval Surface Warfare Center Carderock Division (NSWCCD). NavyFOAM was funded by the Department of Defense High Performance Computing Modernization Program (HPCMP) under the Computational Research and Engineering Acquisition Tools and Environments (CRE-ATETM) Ships Hydrodynamics Program, Office of Naval Research, and internal Naval Innovation Science and Engineering (NISE). NavyFOAM includes a number of features and advanced capabilities such as discretization schemes, advanced turbulence models, single- and multiphase flow solvers and customized post-processing utilities not included in OpenFOAM. The functionalities of NavyFOAM are specifically tailored to naval applications ranging from surface ships (Aram and Kim, 2017) to submarines (Kim et al., 2013), cavitation (Kim and Brewton, 2008), propeller flow analysis (Kim et al., 2010) and surface roughness (Vargas et al., 2019). RANS, LES, and laminar to turbulent transition models (Aram et al., 2022) are also part of NavyFOAM's capabilities. The software was developed with the objective of reducing the length of design cycles for ships but is also used for examining resistance, powering, and manoeuvring. NavyFOAM includes single- and multi-phase RANS flow solvers. NSWCCD used NavyFOAM for Phase 2 computa-

4.3. Phase 1: Initial Predictions

In Phase 1, participants were asked to use their own grids and numerical methods to determine the static stall angle for the AVT-392 rudder, to within one degree or less, given the benchmark conditions specified in Section 3. The minimum range for static α values used in all cases was $20^{\circ} \le \alpha \le 28^{\circ}$, but some participants had to expand that range to capture stall. Seven different institutions performed computations with five different flow solvers for Phase 1, as summarized in Table 4. Various mesh types were used, with cell counts ranging from 11×10^6 to 55×10^6 . In all cases, the first cell layer at the rudder surface was set to resolve the boundary layer to an average y^+ of 1 or less. Most participants used the SST turbulence model, but some used the seven-equation Baseline Reynolds Stress (BSL-RSM) model (Ansys, Inc., 2022) and the $k - \epsilon$ Realizable model (Shih et al., 1994). While this is not the focus of the present paper, DSTG studied the use of a corner flow correction for the SST model implemented in Ansys Fluent in which case a corner flow correction coefficient, C, is indicated; this is considered a separate model from the base SST model, and is not used for the subsequent verification study.

4.4. Phase 2: Verification Study

4.4.1. Grids

The common grids for Phase 2 were generated by DRDC using the commercial meshing software Fidelity Pointwise, Version 18.6R3. A block-structured topology with only hexahedral cells was used for compatibility with all flow solvers. Fig. 6 shows the surface grid on the AVT-392 rudder and nearby floor and wall boundaries, and Fig. 7 shows the block structure used for the inflation region around the rudder. The block structure was carefully constructed around the tip trailing-edge region of the rudder, as shown in Fig. 8, to conform precisely to the rudder geometry while achieving high quality grid metrics (e.g., by avoiding small internal angles and large aspect ratios). Two grid types were generated, as contrasted in Fig. 6: 1) a conformal grid in which there is a 1:1 connection between all cell nodes in the domain, and 2) a nonconformal grid with a sliding interface between a fixed tunnel mesh region and a cylindrical region surrounding the rudder. The cylindrical region spans the entire height of the tunnel domain and is identical

Table 4 Summary of Submissions for Phase 1: Initial Predictions. SST-ns indicates a non-standard version of Menter's $k-\omega$ SST model.

Sub.	Organization	Re_c	Solver	Turbulence model	Mesh type	Cells	Ave. y+
1-1	DRDC	7.44E6	Ansys CFX	SST-2003	Hex	55M	~ 0.4
1-2	MARIN	7.44E6	REFRESCO	SST-2003	Hex	12.6M	~ 0.06
1-3	QinetiQ	7.44E6	STAR-CCM+	SST-ns	Trimmed	$\sim 18M$	~ 0.2
1-4	QinetiQ	7.44E6	STAR-CCM+	SST-ns	Hex	55M	~ 0.2
1-5	Naval Group	7.44E6	STAR-CCM+	SST-ns	Hex dominant	36M	~ 1
1-6	DSTG	7.44E6	Ansys Fluent	SST-2003	Hex/Tet	41M	~ 0.5
1-7	DSTG	7.44E6	Ansys Fluent	SST-2003, $C = 1$	Hex/Tet	41M	~ 0.5
1-8	DSTG	7.44E6	Ansys Fluent	SST-2003, $C = 0.5$	Hex/Tet	41M	~ 0.5
1-9	DSTG	7.44E6	Ansys Fluent	SST-2003, $C = 2$	Hex/Tet	41M	~ 0.5
1-10	DSTG	7.44E6	Ansys Fluent	$k - \epsilon$ Realizable	Hex/Tet	41M	~ 0.5
1-11	DSTG	7.44E6	Ansys Fluent	BSL-RSM	Hex/Tet	41M	~ 0.5
1-12	UNB	7.44E6	Ansys CFX	BSL-RSM	Hex	55M	~ 0.4
1-13	FOI	7.44E6	OpenFOAM	SST-ns	Hex dominant	41M	~ 0.25
1-13	DRDC	1.00E6	Ansys CFX	SST-2003	Hex	55M	~ 0.06
1-14	MARIN	1.00E6	REFRESCO	SST-2003	Hex	10.9M	~ 0.08
1-15	QinetiQ	1.00E6	STAR-CCM+	SST-ns	Trimmed	21M	~ 0.2
1-16	Naval Group	1.00E6	STAR-CCM+	SST-ns	Hex dominant	27M	~ 1
1-17	DSTG	1.00E6	Ansys Fluent	SST-2003	Hex/Tet	41M	~ 0.08
1-18	DSTG	1.00E6	Ansys Fluent	SST-2003, $C = 1$	Hex/Tet	41M	~ 0.08
1-19	DSTG	1.00E6	Ansys Fluent	SST-2003, $C = 0.5$	Hex/Tet	41M	~ 0.08
1-20	DSTG	1.00E6	Ansys Fluent	SST-2003, $C = 2$	Hex/Tet	41M	~ 0.08
1-21	DSTG	1.00E6	Ansys Fluent	$k - \epsilon$ Realizable	Hex/Tet	41M	~ 0.08
1-22	DSTG	1.00E6	Ansys Fluent	BSL-RSM	Hex/Tet	41M	~ 0.08

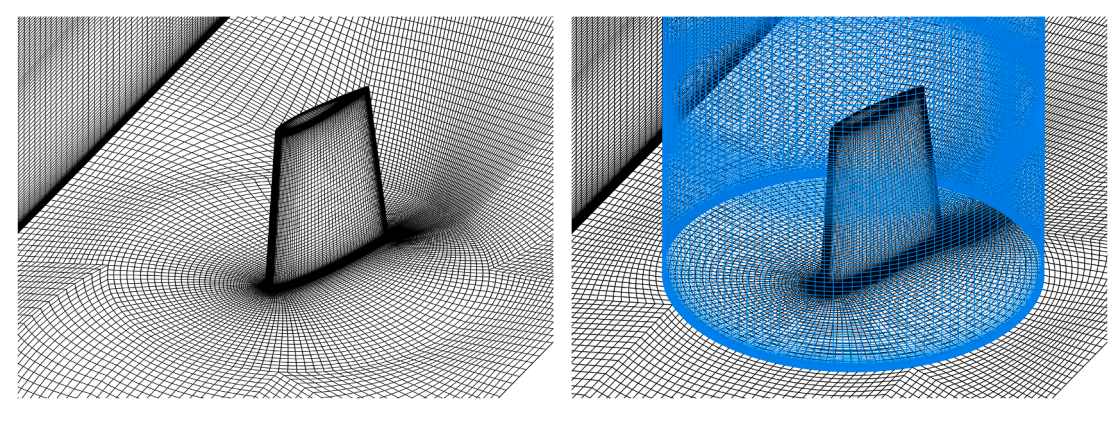


Fig. 6. Coarse surface grid in the vicinity of the rudder, $\alpha = 24^{\circ}$. Left: grid with single, fully-connected domain (grid L4); Right: grid with a sliding interface (blue) between a cylindrical region that rotates with the rudder and a fixed tunnel mesh.

in both the conformal and sliding-interface grids; in both cases it is rotated about the rudder axis to generate different angles of attack. For the conformal grid, the tunnel blocks adjacent to the cylindrical region were skewed such that a 1:1 connection is retained everywhere. For the non-conformal grid, the tunnel mesh outside the cylindrical region remains fixed and the mismatch between grid nodes across the cylindrical interface is handled by interpolation. The sliding interface is convenient for generating α variations directly within a flow solver and can be used for dynamic cases, but it introduces additional numerical uncertainty due to the interpolation. The conformal grids were used by all participants to complete a careful grid study without this complication. The sliding interface was then shown to have a negligible effect on forces and moments for the Ansys CFX flow solver, which was used for simulating many static α near stall and for performing dynamic URANS simulations at quasi-static rudder rotation rates. In order to estimate discretization uncertainties, grids were generated with 6 different refinement levels. The coarsest grid is referred to as the 'L4' refinement level because the number of cells in every block direction is divisible by 4. Finer grids (L5, L6, L8, L10, and L12) were generated with a script that increases the number of cells in the base L4 grid by the refinement ratio (e.g. by 5/4 for 'L5') in all three coordinate directions, while also decreasing the grid spacing by the inverse of the refinement ratio. In this way, the grids formed a geometrically-similar set suitable for estimating discretization

uncertainty. Table 5 summarizes the DRDC grid parameters used in this study. The total cell count ranged from 6.9×10^6 for L4 to 185.5×10^6 for L12.

4.4.2. Summary of Phase 2 computations

In the second phase of this collaborative work, all participants used the DRDC structured grid set and the SST turbulence model. The submissions are summarized in Table 6. The focus for this phase was on a condition that showed significant discrepancies between submissions for the initial study: $\alpha = 24^{\circ}$ at $Re_c = 7.44 \times 10^6$. As will be elaborated in Section 5.3, different initialization methods were investigated as they were found to affect the solution. Computations were done using segregated solvers using the SIMPLE algorithm or some variant of it, except for the DRDC computations with the Ansys CFX coupled solver. The various combinations of explicit and implicit relaxation parameters used for the solutions are tabulated in Table 6. DRDC used a pseudo-transient scheme where a large physical timestep of $\Delta t U_{\infty}/\bar{c}=0.22$ is used to converge the steady RANS equations. MARIN (for one set) and UNB used a URANS approach with a first-order accurate temporal discretization as a means to achieve a steady-state solution - this can also be viewed as a pseudo-transient approach because the unsteady component of the solution was not accurately resolved.

Table 5 Grid parameters for the DRDC grids. The y^+ values were computed with OpenFOAM at $\alpha=24^\circ$ and are for first cell centres (y^+ values for first grid node are double). δ_c and δ_s are the grid spacings in the chordwise and spanwise directions, respectively. N indicates the number of cells in a specified direction.

Grid Refinement Level	L4	L5	L6	L8	L10	L12
Relative step size	3	2.4	2	1.5	1.2	1
Total cells (millions)	6.9	13.4	23.2	55.0	107.3	185.5
Tunnel cells outside cylinder (millions)	4.6	9.0	15.5	36.8	72.0	124.3
Cells in cylinder around rudder (millions)	2.3	4.4	7.6	18.1	35.4	61.2
Cells in rudder inflation (millions)	1.2	2.3	3.9	9.2	18.0	31.2
N around airfoil	176	220	264	352	440	528
N over rudder span	120	150	180	240	300	360
<i>N</i> inflation (within $\approx 0.09\bar{c}$ of rudder)	48	60	72	96	120	144
$\delta_c/\bar{c} \times 100$ at root leading edge	0.35	0.28	0.23	0.17	0.14	0.12
$\delta_c/\bar{c} \times 100$ at root trailing edge	0.081	0.065	0.054	0.040	0.032	0.027
$\delta_c/\bar{c} \times 100 \text{ maximum}$	3.65	2.92	2.43	1.82	1.46	1.21
$\delta_s/\bar{c} \times 100$ at tip	0.087	0.070	0.058	0.044	0.035	0.029
$\delta_{\rm s}/\bar{c} \times 100 {\rm maximum}$	3.76	3.00	2.49	1.87	1.49	1.24
First grid node height, rudder, $y_1/\bar{c} \times 10^6$	2.7	2.1	1.8	1.3	1.1	0.9
First grid node height, floor, $y_1/\bar{c} \times 10^6$	4.4	3.5	3.0	2.2	1.8	1.5
Rudder average y^+ , $Re_{\bar{e}} = 7.4 \times 10^6$	0.41	0.33	0.27	0.19	0.16	0.13
Rudder max. y^{+} , $Re_{\bar{c}} = 7.4 \times 10^{6}$	1.2	1.0	0.80	0.60	0.49	0.40
Cell expansion rate at rudder	1.221	1.173	1.142	1.104	1.083	1.069
Cell expansion rate at tunnel floor	1.191	1.151	1.124	1.092	1.073	1.061
Minimum cell internal angle (degrees)	39.3	38.9	38.5	38.2	38.0	37.9
Maximum cell aspect ratio	3.4×10^4					
Maximum cell volume ratio	2.1	1.9	1.9	1.9	1.9	1.9

Table 6 Summary of static submissions for Phase 2 grid study, for $\alpha = 24^{\circ}$ at $Re_c = 7.44 \times 10^6$. The relaxation parameters listed are for the momentum (Mom), turbulence (Turb) and pressure correction (P) equations, with the tags E and I indicating explicit and implicit relaxation, respectively.

Sub	Org.	Solver	Solver method	Initialization	Relaxation Parameters Explicit (E) or Implicit (I)
2-1a	MARIN	REFRESCO	SIMPLE-like	$u = U_{\infty}$ or restart	Mom,Turb: 0.975 <i>I</i> , 0.3 <i>E</i> ; P:0.15 <i>E</i>
2-1b	MARIN	REFRESCO	SIMPLE-like	$u = U_{\infty}$ or restart	1st order URANS, $\Delta t U_{\infty}/\overline{c} = 1/50$
2-2	Naval Group	STAR-CCM+	SIMPLE-like	$u = U_{\infty}$	Mom:0.71; Turb:0.81; P:0.3E
2-3	DRDC	Ansys CFX	coupled	$u = U_{\infty}$	Pseudo-transient, $\Delta t = 0.01s$
2-4	CNR-INM	OpenFOAM	SIMPLE	Potential Flow	Mom:0.9E; Turb:0.7E; P:0.7E
2-5	UNB	Ansys Fluent	PISO	Potential Flow	1st order URANS, $\Delta t U_{\infty} / \overline{c} = 1/25$
2-6	QinetiQ	STAR-CCM+	SIMPLE-like	Inviscid Euler	Mom:0.51; P:0.2E
2-7	Chalmers	STAR-CCM+	SIMPLE-like	Low μ , $u = U_{\infty}$	Mom:0.71; Turb:0.81; P:0.15E
2-8	NSWCCD-p	NavyFOAM	SIMPLE	Potential flow	Mom:0.2E; Turb:0.2E; P:0.3E
2-9	NSWCCD-v	NavyFOAM	SIMPLE	$u = U_{\infty}$	Mom:0.2E; Turb:0.2E; P:0.3E

Table 7 Summary of static submissions for Phase 2 over a range of α at $Re_c = 7.44 \times 10^6$.

Sub/Org	Solver	Initialization	Range	Relaxation Parameters or Timestep
MARIN DRDC-a DRDC-d UNB-a UNB-d	REFRESCO Ansys CFX Ansys CFX Ansys Fluent Ansys Fluent	$u = U_{\infty}$ or restart $u = U_{\infty}$, low μ for $\alpha > 26^{\circ}$ $u = U_{\infty}$, high μ Potential Flow $u = U_{\infty}$, high μ	$18^{\circ} \le \alpha \le 24^{\circ}$ $20^{\circ} \le \alpha \le 27.5^{\circ}$ $25^{\circ} \le \alpha \le 27.5^{\circ}$ $18^{\circ} \le \alpha \le 27^{\circ}$ $25.5^{\circ} \le \alpha \le 27.5^{\circ}$	See Sub 2-1a and 2-1b of Table 6 Pseudo-transient, $\Delta t U_{\infty}/\bar{c} = 0.22$ 2nd order URANS, $\Delta t U_{\infty}/\bar{c} = 1/32$ 1st order URANS, $\Delta t U_{\infty}/\bar{c} = 1/25$ 1st order URANS, $\Delta t U_{\infty}/\bar{c} = 1/25$

Some participants ran simulations with the *DRDC* grids over a range of static α at $Re_c=7.44\times10^6$, as summarized in Table 7. *MARIN* used the L10 grid and the same methodology as in the grid study to compute solutions for $18^\circ \le \alpha \le 24^\circ$. The *DRDC*-a and *UNB*-a computations were run at angles up to stall with methods that produced an attached-flow solution. For *UNB* this was achieved using potential flow initialization and URANS with first order temporal discretization. For *DRDC*, initialization with the free-stream velocity and a pseudo-transient solution method could only produce an attached-flow solution up to $\alpha=26^\circ$. Beyond that, simulations were initialized using a low fluid viscosity to first establish an attached flow solution at higher Reynolds number. The viscosity was then increased in steps until the true fluid viscosity was

set, and then the computations run for many convection times to see if the attached-flow solution persisted or if the flow detached. The opposite approach was taken for the *DRDC*-d and *UNB*-d series: simulations were initialized using a high fluid viscosity in order to first establish a detached-flow solution at a lower Reynolds number and then the viscosity was reduced in a step change to the true fluid viscosity and held for several convection times to see if the flow remained detached or progressed to an attached-flow solution. In this way, the *-a and *-d series were used to determine the upper and lower branches, respectively, of a static hysteresis loop for the rudder. The L5 grid was used for all the *UNB* computations. Several grid levels were used for the *DRDC*-a computations to estimate discretization uncertainty.

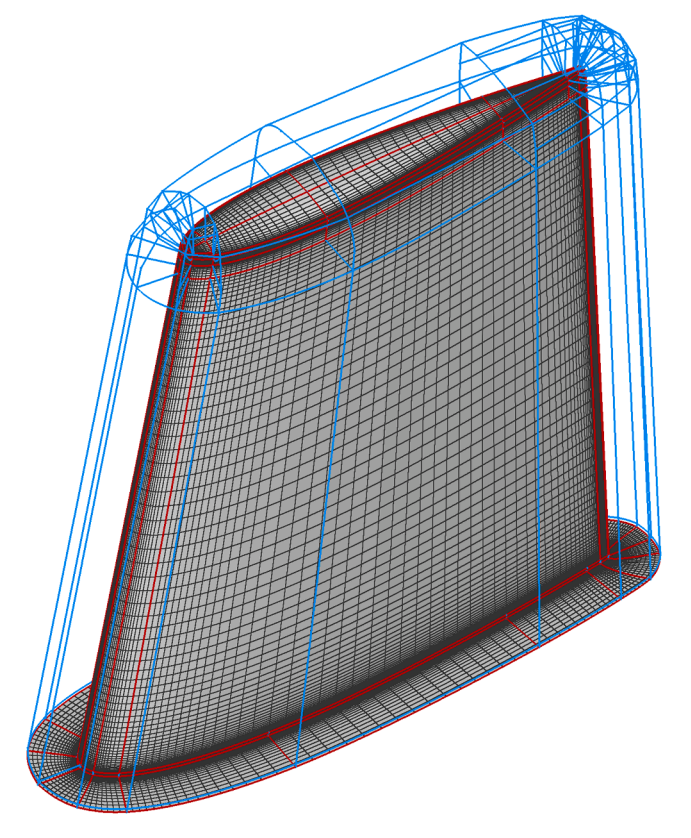


Fig. 7. Inflation block structure around the rudder. Mesh lines are for the coarsest (L4) grid.

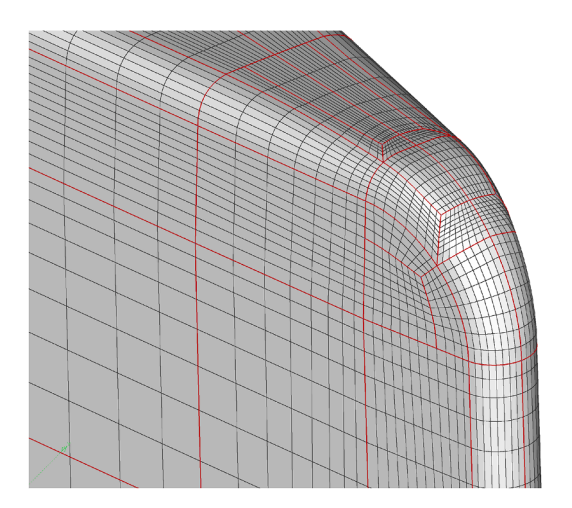


Fig. 8. Surface mesh detail at the tip trailing-edge of the L4 grid.

5. Results

5.1. Global flow field analysis

Prior to discussing specific results for the two phases of work, a qualitative analysis of the global flow field will be presented to characterize different numerical solutions. In this section, we show this with the *UNB* Ansys Fluent results with grid L5 for consistency but note that all the primary flow features are also observed with other solvers and grid refinement levels. Fig. 10 shows the vortex cores in the flow, visualized by non-dimensional Q-criterion isosurfaces, for three separate angles of attack. The three angles of attack demonstrate different stall regimes in

the high angle of attack range. The first, in Fig. 10(a), shows the high- α flowfield below the critical stall angle. Below this angle, the boundary layer is fully attached along the chord, and a dominant tip vortex separates from the leading edge of the rudder. The separated tip vortex produces a suction region on the upper leeside of the rudder, increasing the local normalized lift distribution in the tip region, as shown in Fig. 11. A root trailing edge junction vortex separates from the surface of the rudder. Aft of the trailing edge, the root trailing edge junction vortex combines with the leeside leg of the horseshoe vortex formed at the leading edge root junction.

As the angle of attack increases, the junction vortex moves further towards the trailing edge of the rudder, where at the critical stall angle $(\alpha=24^\circ)$ it degenerates into a small separated shear layer region on the trailing edge, as illustrated in Fig. 9. The boundary layer separation region on the trailing edge continues to increase above the critical stall angle, and this may be classified as light stall. In the light stall region there is no considerable change in the normalized lift distribution, despite the growing region of separated flow. Above the critical stall angle the numerical flowfield is unstable with respect to solution strategy, and the separated flow region has a tendency to interact with the tip vortex, where the solution will then degenerate into a massively separated flow region.

At a second critical stall angle, classified as total or deep stall, it is not possible to obtain an attached flow in quasi-steady conditions, regardless of solution strategy. Generally, if the flowfield degenerates to the deeply stalled state, it is difficult to retrieve the light stall flow until the angle of attack is decreased below the initial critical stall angle. In the deep stall region, the trailing edge boundary layer separation progresses all the way to the leading edge, and interacts strongly with the rudder tip vortex, as shown in Fig. 10(c). This is associated with a dramatic decrease in lift across the span, as shown in Fig. 11, and the lift characteristics are highly dependent on angle of attack. The massively separated region exhibits a periodic vortex shedding tendency and disrupts the horseshoe vortex, which could lead to a significant increase in flow generated noise.

5.2. Initial Study Results

Fig. 12 shows the lift coefficient predicted by all participants in the initial study. A reasonable agreement is obtained for the lift curve prior to deep stall and there is consensus that the stall angle, α_s (which is taken to be the α that gives a maximum C_L in this case), increases with Reynolds number. For a given solution method (participant/solver/turbulence model combination), α_s is typically around 2-3 degrees larger at $Re_c = 7.44 \times 10^6$ than at $Re_c = 10^6$. However, at both Reynolds numbers, there is a very large variation in the actual value predicted for α_s ; it varies from 18° to 24° at $Re_c = 10^6$ and from 22° to 27° at $Re_c = 7.44 \times 10^6$. There is also a large scatter in predicted lift beyond stall, but this is less surprising given the known challenges of steady RANS methods predicting massively-separated flows shown by the deep stall contour in Fig. 9. In many cases, the lift just beyond stall is approximately half that of the value just before stall. The variation in stall angle can have a significant impact on hydrodynamic loads for manoeuvring predictions at high angles of attack, similar to what was observed for the NATO AVT-301 collaboration with the generic BB2 submarine (NATO AVT-301 Task Group, 2022). It is particularly troubling that there is a large scatter in predicted stall angle for computations done with, nominally, the same SST turbulence model (5° variation at $Re_c = 10^6$ and 4° at $Re_c = 7.44 \times 10^6$). However, the objective was to define the new rudder to be suitable for wind tunnel experiments and perform this initial study to see if the scatter observed in AVT-301 could be replicated with a single rudder, and this indeed is the case. This allows us to study this issue with finer grids and higher Reynolds numbers than is possible with a full submarine geometry, as described next.

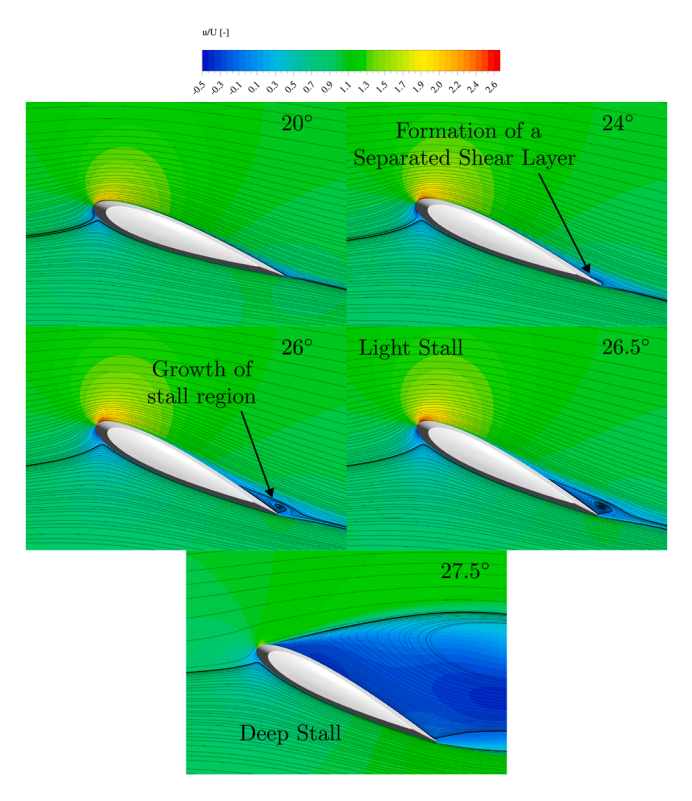


Fig. 9. Flow streamlines and normalized axial velocity contour in the XY plane at a height of $z/\bar{c} = 0.31$. Results are for *UNB*'s computations using Ansys Fluent.

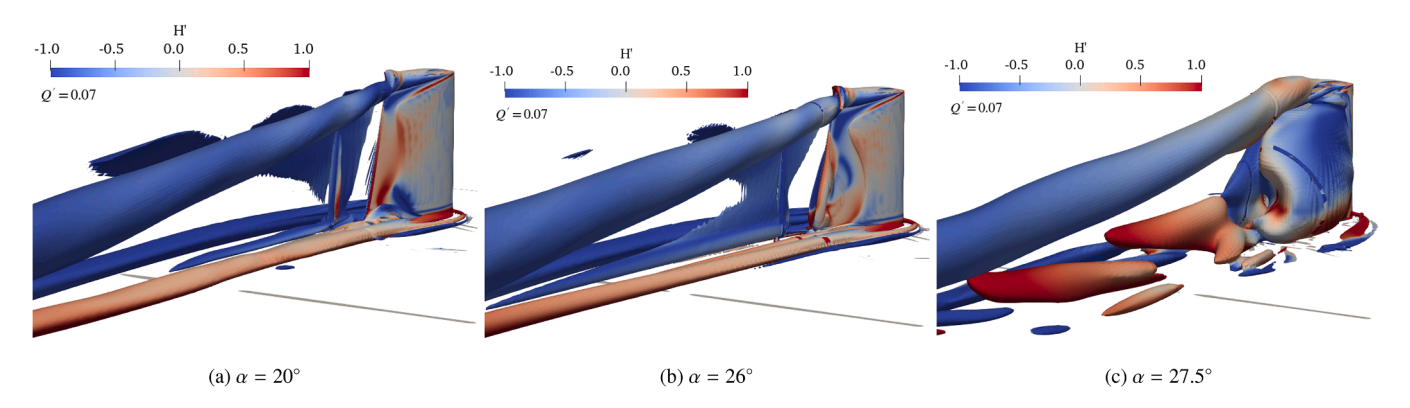


Fig. 10. Vortex cores in the wake of the rudder in three separate flow regimes, a) Attached flow, b) Light stall, c) Deep stall. Q-criterion surface (Q' = 0.07) is coloured by normalized helicity. Results are for *UNB*'s computations using Ansys Fluent with the L5 grid.

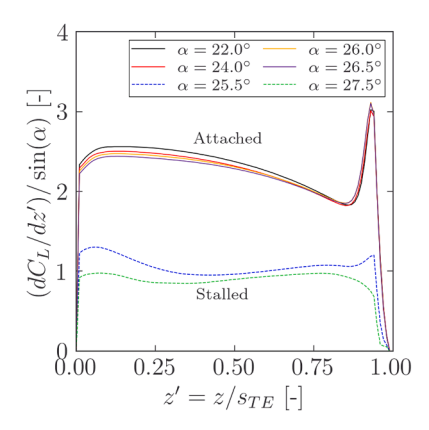


Fig. 11. Normalized lift distribution along the span of the rudder at several angles of attack. Solid lines correspond to the attached flow condition, and dashed to the stalled condition. Results are for *UNB*'s computations using Ansys Fluent with the L5 grid.

5.3. Effects of initialization and solution method

An angle of attack of 24° at $Re_c = 7.44 \times 10^6$ was selected for detailed analysis using the common grid set because this condition produced the largest scatter in Phase 1 predictions. It was discovered that two solutions could be obtained with some solvers for this condition, depending on the initialization method. This is clearly seen by the NavyFOAM results produced by NSWCCD in Fig. 13. The NSWCCD-p computations, which were initialized with a potential flow solution, showed a smooth progression in C_L from around zero to a steady solution of $C_L \approx 1.3$ for all 4 grid refinements considered. The iterations required for forces to reach a steady state increased from 1000 to 4000 as the grid refinement was increased from L4 to L8. In contrast, the NSWCCD-v computations, which were initialized with the free-stream velocity, had very large oscillations in C_L of up to almost ± 200 during the first 50 iterations. The solution started to settle towards $C_L \approx 1.1$ after a few hundred iterations, but then decreased towards a low \mathcal{C}_L of around 0.7 after tens of thousands of iterations. It appears that a steady mean \mathcal{C}_L was established by the end of the NSWCCD-v computations but there were persistent oscil-

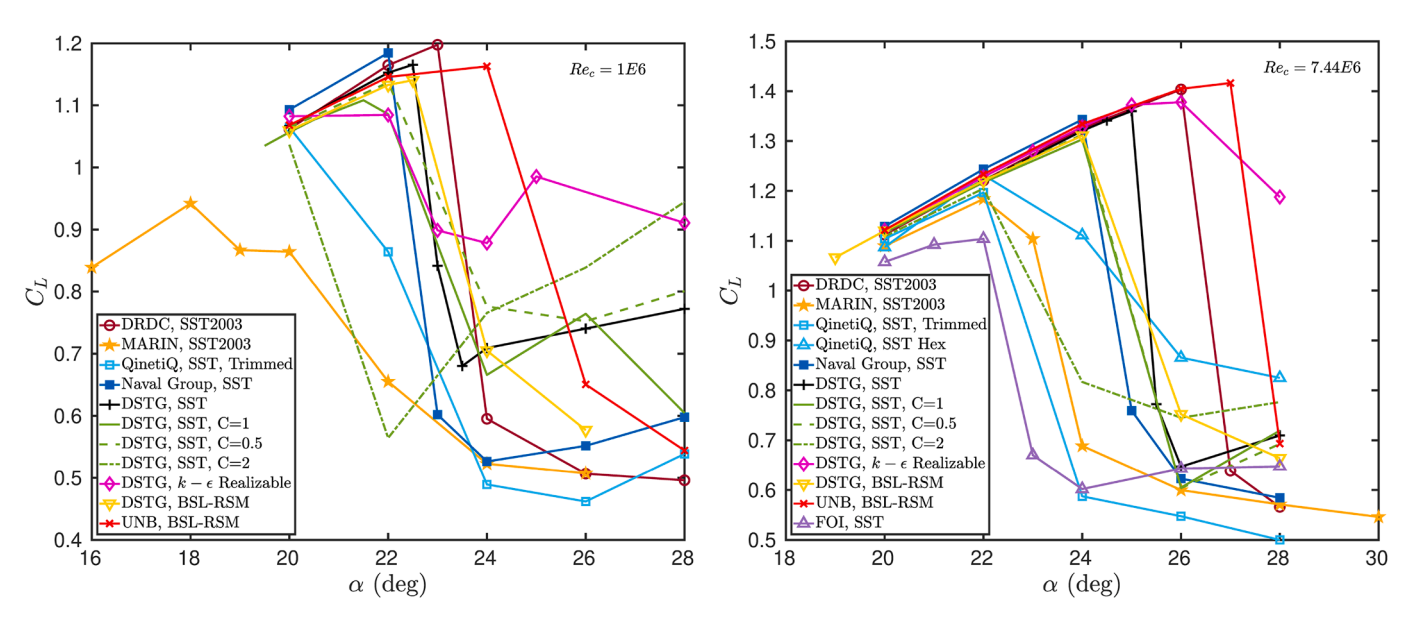


Fig. 12. Initial lift coefficient predictions for Phase 1 of the benchmark study.

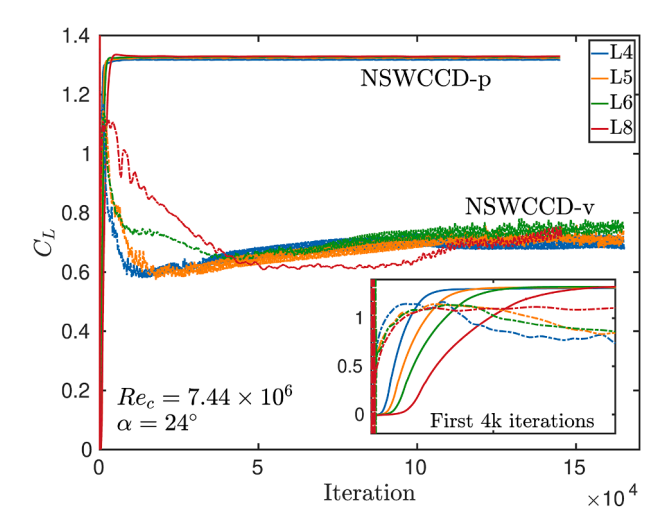


Fig. 13. Convergence of C_L for *NSWCCD* computations with *NavyFOAM*. *NSWCCD*-v (dashed) computations were initialized with the free-stream velocity and the *NSWCCD*-p (solid) computations were initialized using a potential flow solution. The grid refinement level (L4-L8) is indicated by the color of the curves in the legend. Inset: first 4000 iterations.

lations in C_L from iteration-to-iteration of around $\pm 3\%$, indicating that the solution is not well-converged to a steady-state. Note that relatively small relaxation parameters were used for momentum and turbulence equations (see Table 6), which likely suppressed oscillations and slowed convergence relative to other computations. The NSWCCD-p computations produced an attached flow with a small separated flow region, like that shown for 24° in Fig. 9, whereas the result for NSWCCD-v is like the "deep-stall" fully-detached flow shown in the same figure. The oscillations in C_L for NSWCCD-v may be a result of deep-stall unsteady effects.

Like *NSWCCD*-p, *UNB*'s Ansys Fluent computations were initialized with a potential flow method, but in this case, a URANS method with first-order temporal discretization was used. However, the variation of C_L with timestep shown in Fig. 14 is remarkably similar to the shape of the C_L convergence curve for the *NSWCCD*-p computations. Fig. 15 shows the velocity field generated by the potential flow calculation used for initialization in Ansys Fluent in comparison with the converged

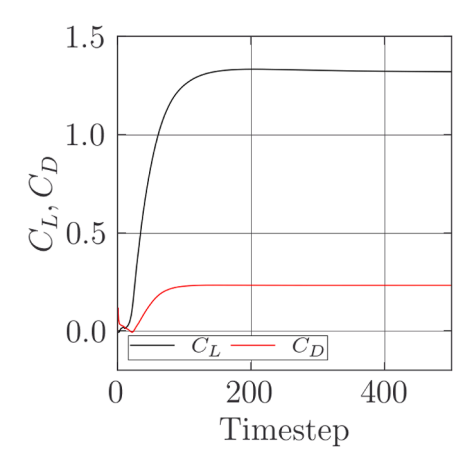


Fig. 14. Convergence of C_L and C_D for the *UNB /* Ansys Fluent computation for $\alpha=24^\circ$ at $Re_c=7.44\times10^6$ with grid L5.

RANS solution (this is for a larger angle of attack than used in the grid study, but the characteristics are the same at lower α). This clearly shows that the potential flow solution provides a much better approximation to the attached-flow viscous solution than the uniform free-stream.

Consistent with NSWCCD-v, MARIN obtained a stalled result for a steady REFRESCO computation with the L4 grid when using the undisturbed free-stream velocity for initialization. However, when this was re-run with URANS, initialized by the low- C_L steady RANS result, a high-lift solution was obtained, as shown in Fig. 16. The URANS result was then used to initialize a steady RANS calculation and the flow remained steady and attached. This clearly indicates that the solution obtained depends on the flow initialization. MARIN obtained solutions for the other grids, L5 up to L12, by restarting from the attached flow solution on coarser grids. In each case, the attached flow solution was maintained. It should be emphasized that, similar to the NSWCCD-v results, MARIN's steady RANS computation did not actually full converge to a steady-state, as can be seen by the force oscillations at the end of the computation. This, combined with the fact that switching to URANS produced a very well-converged steady high-lift solution, indicates that the deep-stall steady RANS result is not a correct solution for $\alpha = 24^{\circ}$ at $Re_c = 7.44 \times 10^6$. We provide further evidence of this in the remainder of this paper.

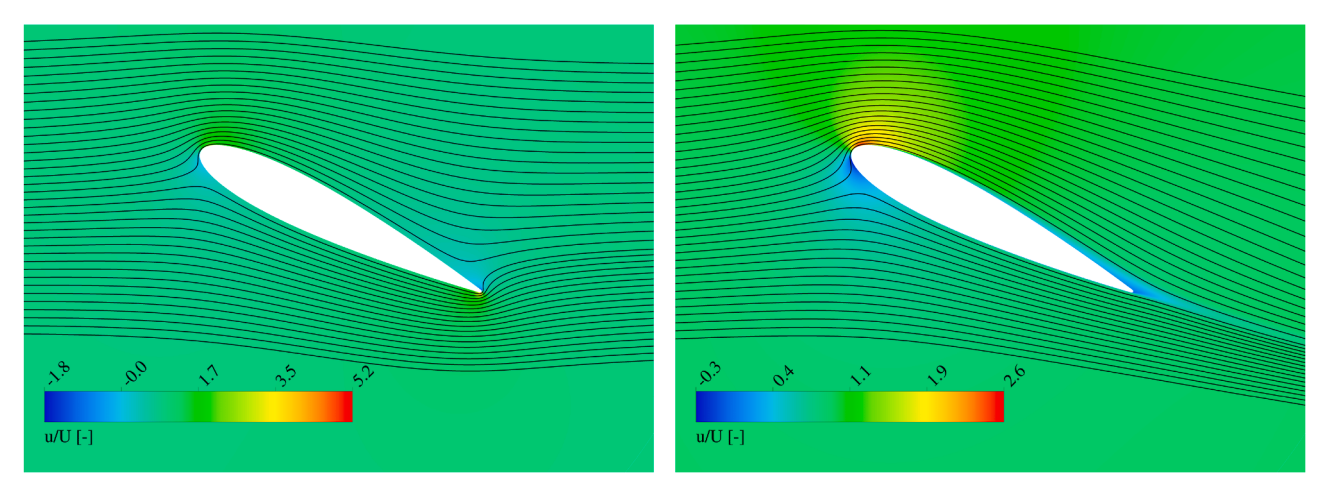


Fig. 15. Velocity contour and streamlines at $z/\bar{c} = 0.887$ predicted by the *UNB* / Ansys Fluent potential-flow solution used for initialization (left) and RANS solution (right) for $\alpha = 26.5^{\circ}$, $Re_c = 7.44 \times 10^6$, grid L5.

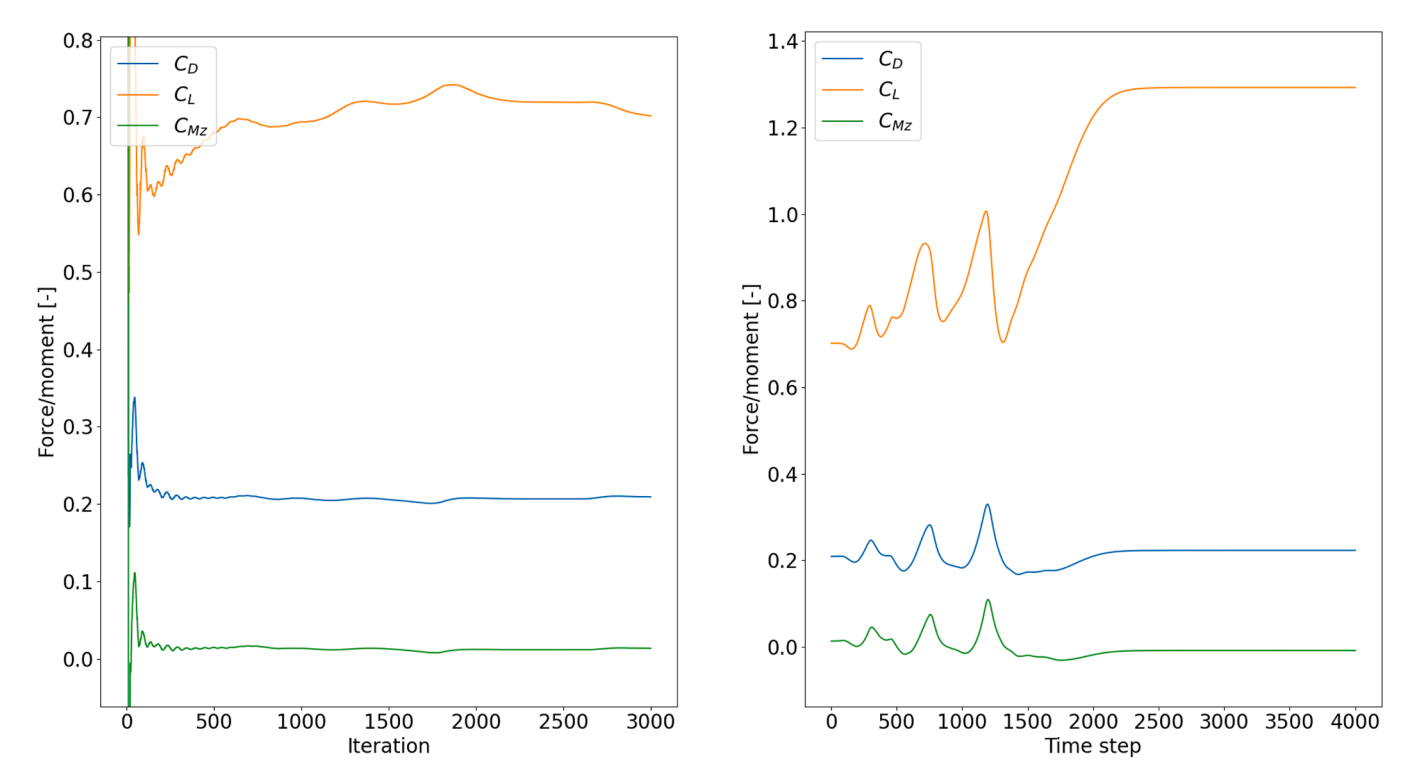


Fig. 16. Force history for *MARIN* computations with REFRESCO at $\alpha = 24^{\circ}$, $Re_c = 7.44 \times 10^6$ using the L4 grid. Left: steady RANS initialized with the uniform free-stream; right: URANS initialized from the RANS solution.

Chalmers and Naval Group also used the undisturbed free-stream velocity as initialization for STAR-CCM+ computations. They initially observed a low C_L after several solver iterations, indicative of deep-stall, similar to MARIN's REFRESCO computations. However, when run for many iterations, the computations eventually arrived at the high-lift solution in most cases. This is demonstrated for the L6 grid in Fig. 17(a). A low C_L was established after a few thousand iterations and then it very slowly increased over the next 40000 iterations, at which point there was a relatively quick transition to a steady high-lift solution. This shows that a seemingly-converged low-lift solution can be obtained if a computation is ended early (at iteration 10000 for example). However, the high-lift solution could not be achieved for the Chalmers computations with the two finest grids considered (L8 and L10) after many iterations. For these cases, Chalmers found that an attached-flow solution could be obtained by initializing the fluid viscosity with a value of 1%

of the nominal air viscosity then increasing it to the true air viscosity using two ten-fold step increases. As shown in Fig. 17(b), this process first establishes steady high-lift solutions at the higher Reynolds numbers that correspond to the lower viscosity settings. There were some disturbances in the forces when the viscosity was changed, but this process enabled a satisfactory convergence to an attached flow solution at $Re_c = 7.44 \times 10^6$.

The Ansys CFX computations done by *DRDC* also used free-stream initialization. High-lift, attached flow results were obtained for all grids. There were large initial oscillations in forces, followed by a drop in C_L towards the value for detached-flow, similar to the other computations initialized with free-stream velocity. However, the lift then increased towards a large steady value in a manner similar to the *MARIN* URANS computation shown in Fig. 16. This similarity is not surprising because the *DRDC* computations used a pseudo-transient method. A large pseudo

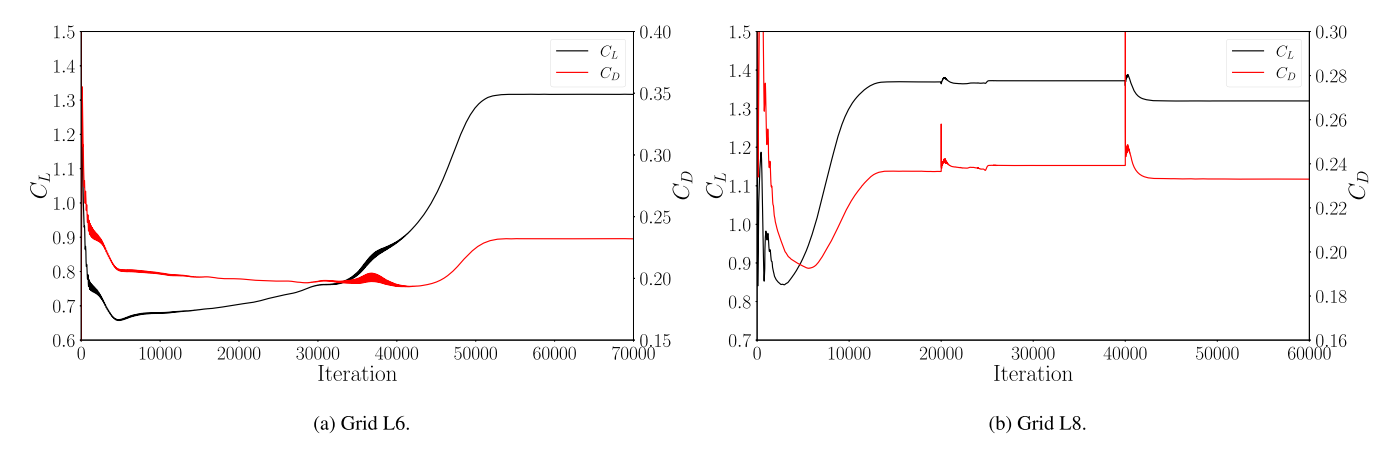


Fig. 17. Force convergence for *Chalmers*' computations with STAR-CCM+ at $Re_c = 7.44 \times 10^6$, $\alpha = 24^\circ$. Computations were initialized using the uniform free-stream velocity. For grid L8, the viscosity was adjusted from $\mu/100$ (first 20000 iterations) to $\mu/10$ (iterations 20001 to 40000) to μ (iterations 40001 to end).

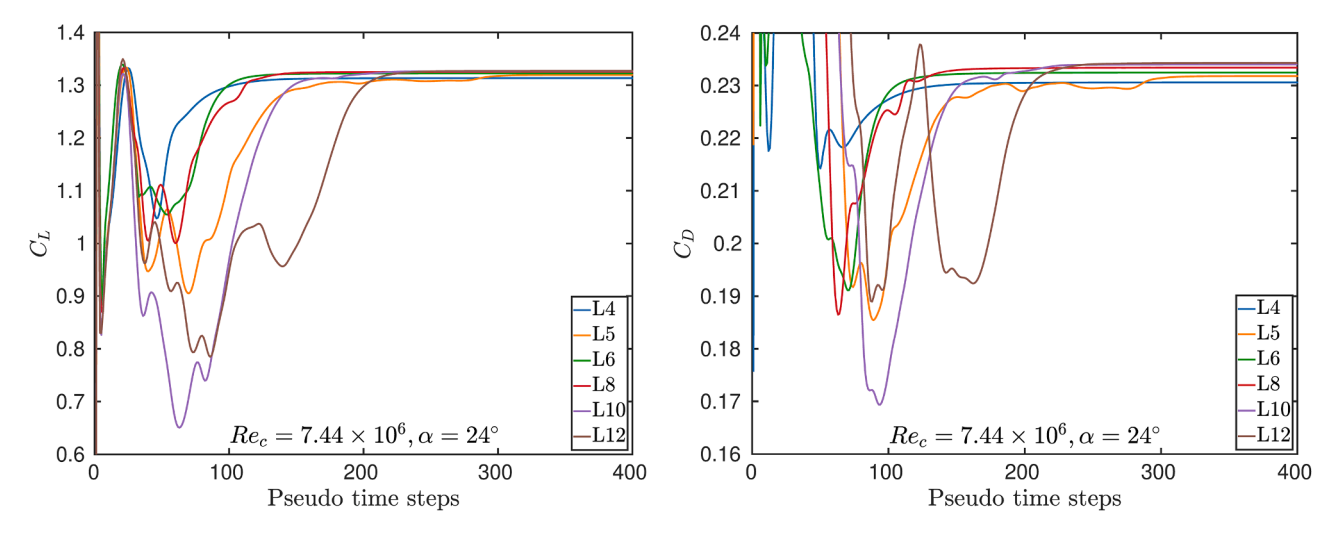


Fig. 18. Convergence of C_L and C_D for DRDC computations with Ansys CFX at $\alpha = 24^\circ$, $Re_c = 7.44 \times 10^6$.

timestep of $\Delta t U/c=0.22$ was found to be stable with the Ansys CFX coupled solver, which enabled the forces to converge to steady values in around 200 pseudo-timesteps. The computations were continued until the L_{∞} -norm residuals for continuity and momentum fell below 10^{-6} , for all grids. As a test, the L_{∞} residuals for all equations were reduced to below 10^{-14} for the L8 grid. When the 10^{-6} convergence criterion was reached, the lift, drag, and yawing moment were converged to within 0.0001%, 0.0014%, and 0.072% of the final values, respectively. These iterative errors are approximately three orders of magnitude smaller than the estimated discretization uncertainty (discussed in the next section), so they have a negligible contribution to the overall numerical uncertainty.

The other grid study submissions (*CNR-INM*/OpenFOAM, and *QinetiQ*/STAR-CCM+) used an inviscid solver (either potential flow or Euler) to initialize the flow. They produced steady attached-flow results like *NSWCCD*-p, with the exception that the *QinetiQ*/STAR-CCM+ computations produced a stalled result for the L4 grid. This result is omitted from the discretization uncertainty analysis described next as it is clearly in a different flow regime than results for other grids. A similar study was conducted for $\alpha = 22^{\circ}$ at $Re_c = 1 \times 10^6$ and the same trends were observed in terms of the effect of initialization and solution strategy.

Note that the strategy used to obtain an attached flow solution was based on the available methods in each flow solver. Additional strategies are possible, such as using a converged solution at a smaller α for initialization. This was tested by one participant but found to require excessively small changes in α . This is because the rudder boundary must

be rotated relative to the fixed tunnel side walls in order to change α (whereas the free stream velocity could be adjusted if the rudder were in a free-field), and the required interpolation did not provide a smooth enough re-start with 0.5 degree increments. The rudder could also be rotated dynamically in an unsteady simulation, but this should be done with a reduced rotation rate of less that 10^{-4} to approximate quasi-static conditions (Le Fouest et al., 2021). This results in an expensive computation with many timesteps if a large range of α is to be explored using a reasonable Courant number. In Section 5.6, we use this dynamic method to evaluate a hysteresis loop.

5.4. Discretization uncertainty analysis

Discretization uncertainty estimates were made for attached-flow solutions using the least-squares method of Eça and Hoekstra (2014) that was updated in 2023 (Eça et al., April 2023) and implemented in a computer program distributed by *MARIN* (Maritime Research Institute Netherlands, 2025). In this method, least-squares regression is used to fit a power-series to a solution variable, ϕ , as a function of the grid refinement ratio, $r_i = h_i/h_1$, where h_i is the grid spacing for grid i, and i = 1 for the finest grid. First, the preferred fit of the form $\phi = \phi_0 + \alpha h^p$ is evaluated, where ϕ_0 is the exact solution in the limit of zero mesh spacing, α is the error constant, and p is the observed order of convergence. If p is not in the acceptable range of $0.5 \le p \le 2.05$, then the best of three alternative fits is used instead: a linear fit (p = 1), a single-term quadratic fit (p = 2), or a two-terms fit ($\phi = \phi_0 + \alpha_1 h + \alpha_2 h^2$). How-

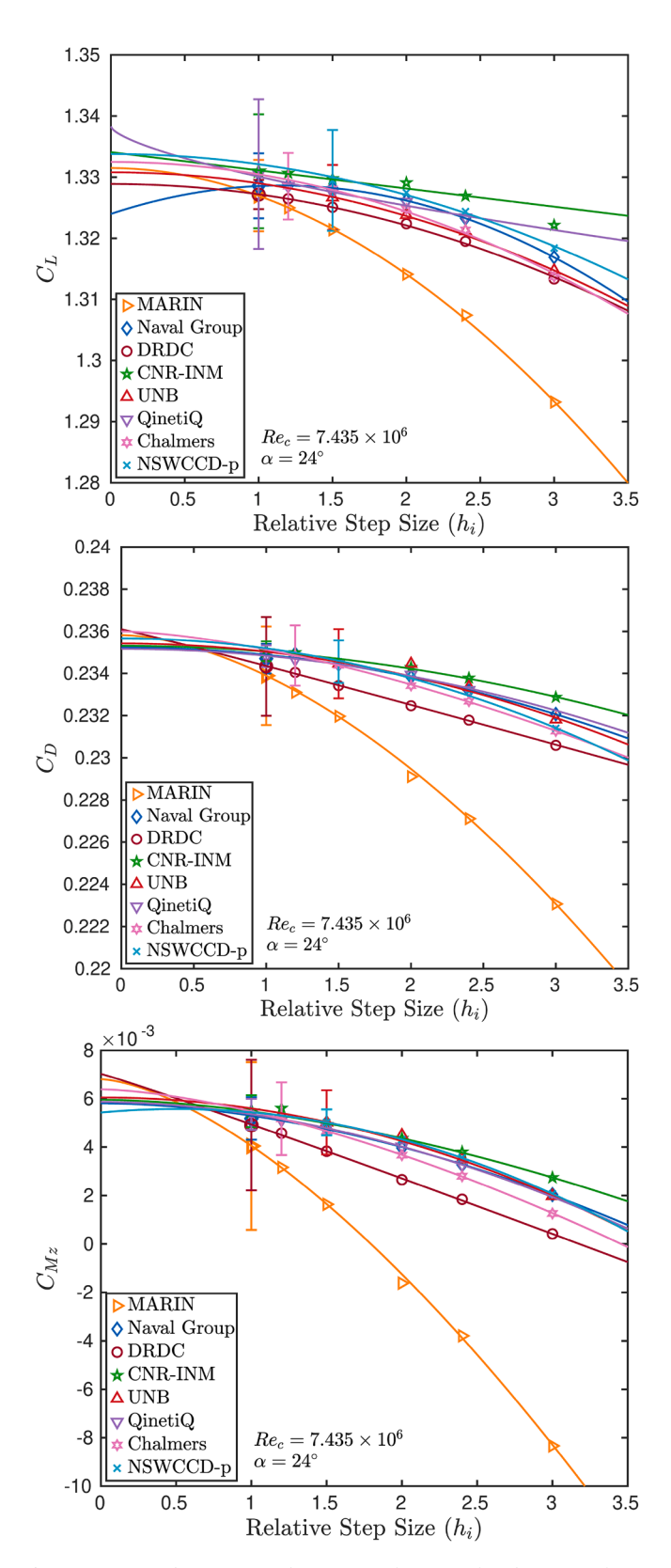


Fig. 19. Force and moment predictions as a function of grid step size for attached flow results. The curves are least-square fits to each series, and the error bars show the estimated discretization uncertainty for the finest grid in a series.

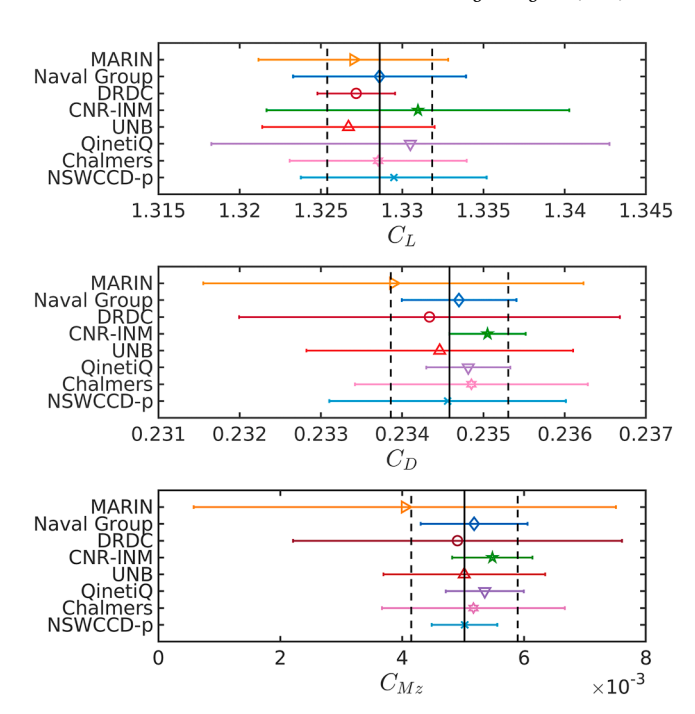


Fig. 20. Comparison of fine mesh force and moment predictions for $Re_c = 7.44 \times 10^6$, $\alpha = 24^\circ$. The mean and ± 2 standard deviations of submission results are shown by black solid and dashed lines, respectively.

ever, the two-terms fit is only considered if its standard deviation is smaller than 5% of the average data change, $\Delta\phi=(\phi_{max}-\phi_{min})/(n_g-1)$, where n_g is the number of grids used for the fit. The error estimate, $\phi_i-\phi_0$, is multiplied by a factor of safety (that depends on the quality of the fit) to obtain a discretization uncertainty estimate for the solution with grid i. The standard deviation of the fit itself is also included in the uncertainty estimate.

All attached-flow results for C_L , C_D , and C_{Mz} are shown as a function of grid refinement ratio in Fig. 19. In these plots, the step size is normalized by the finest grid, L12, which is assigned a step size of h = 1. The coarsest grid, L4, has a relative step size of h = 3 because its cell edge lengths are 3 times those of the L12 grid throughout the domain. The error bars show the calculated discretization uncertainty for the finest grid in each submission, which ranges from grid L8 to L12. Overall, there is good agreement between all 8 submissions in terms of both the fine grid solution and the trends with grid refinement. In general, the lift and drag increase in magnitude monotonically as the mesh is refined (step size is reduced). A notable exception is the Naval Group results for C_{I} . for which a two-term fit was obtained that has a decreasing trend in the extrapolation towards zero step size, h = 0. A similar, but less noticeable trend was obtained for the NSWCCD-p results for C_{Mz} . In all other cases, single-term fits were obtained for lift, drag, and yawing moment. The exponents used for the fits, p, are given along with uncertainty estimates for the finest and L5 grid solutions for each series in Table 8. In many cases, a fit with p = 2, or close to 2, was obtained, consistent with the expect order of convergence for second order methods, but in some cases the observed order of convergence was closer to linear (p = 1). In all cases, the estimated discretization uncertainties for the fine grid solutions was below 1% for C_L and below 2% for C_D . The uncertainty in C_{Mz} appears large as a percentage, but that is because its magnitude is very small for this condition. This is because the yaw axis is located at the quarter-chord (at mid-span), which is the theoretical position of centreof-lift in thin airfoil theory. Later, it will be shown that C_{Mz} increases to around 0.05 for a stalled condition, which is an order of magnitude larger than the value predicted for these pre-stall results. When normalized by this post-stall value, the fine-grid uncertainties for \mathcal{C}_{Mz} are in the range of around 1 - 7%.

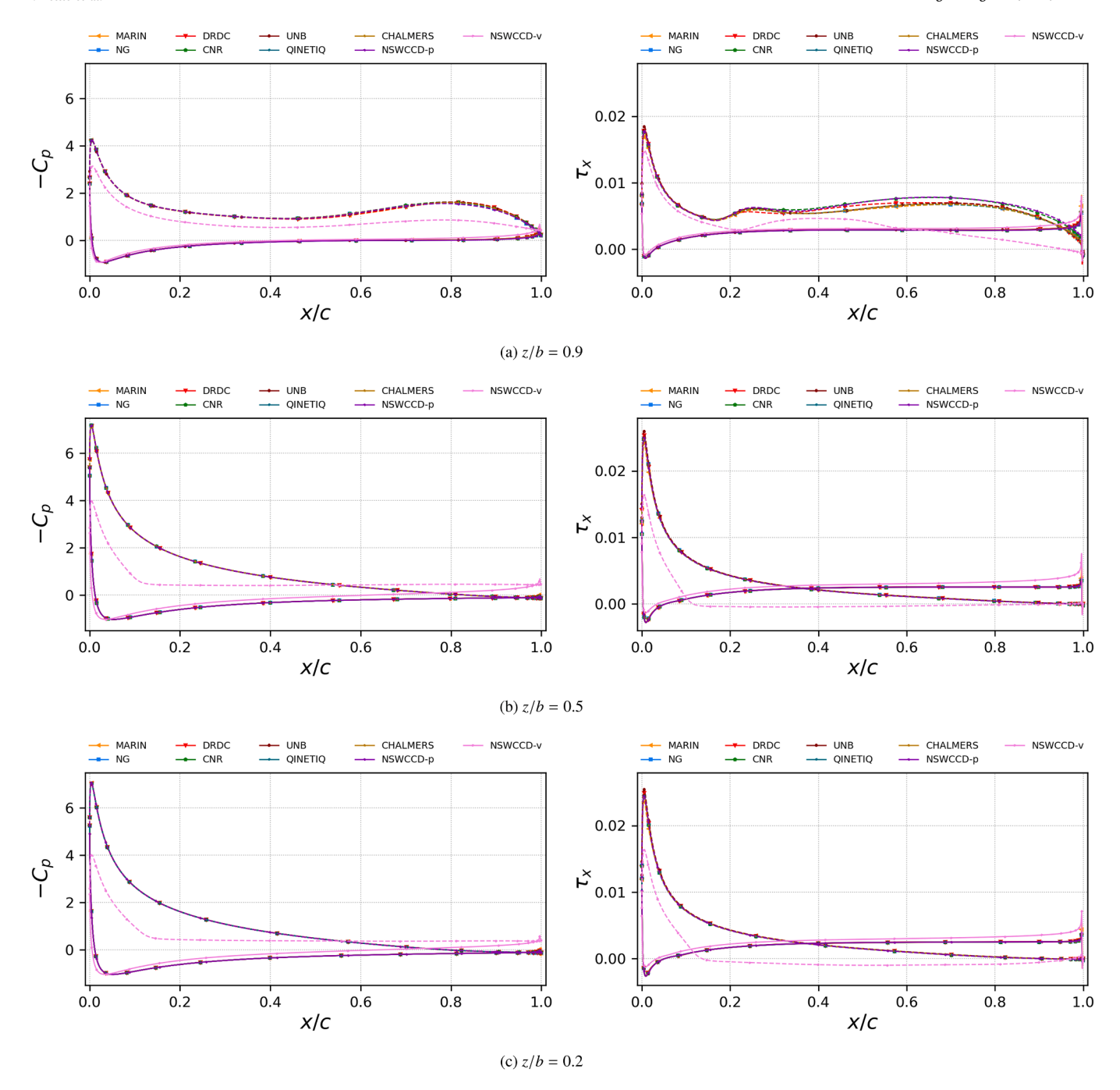


Fig. 21. Grid L8 predictions of c_p and non-dimensional x-component of wall shear, τ_x' , as a function of local chord at 3 spanwise locations for $\alpha=24^\circ$ at $Re_c=7.44\times10^6$. Dashed lines: suction side; solid lines: pressure side.

The predicted uncertainties for the L5 grid are included in Table 8 because this level of refinement may be of practical interest when meshing an entire marine vehicle. This grid, which contains 4.4×10^6 cells in the cylindrical region surrounding the rudder (as opposed to 61.2×10^6 for the L12 grid), gives estimated discretization uncertainties as low as 1% for both C_L and C_D for cases where a single-term fit was applied. The largest uncertainty was 2.4% for C_L and 4.8% for C_D . Note that an unexpectedly-low uncertainty estimate was obtained for the Naval Group result, for which a two-term fit was applied. This is because the result for the L5 grid (h=2.4) happens to be very close to the extrapolation to h=0 in this case. The two-term fit shows anomalous convergence behaviour that could be due to the results being outside of the asymptotic range and/or the cancellation of errors in the surface integration process used for calculating integral quantities. As such, these coarse-grid

uncertainty values for the cases with two-term fits should not be used as general guidance for the accuracy of the L5 grid. Also note that each code has a different error constant but the extrapolation to h=0 ('infinite refinement') is consistent. This highlights the fact that there are different grid requirements for each solver and it is thus best to perform a discretization uncertainty analysis for a given geometry/problem and flow solver.

Fig. 20 compares the finest grid results for all the submissions with error bars showing the estimated discretization uncertainties for these results. Since all error bars overlap with each other for all quantities of interest $(C_L, C_D,$ and $C_{Mz})$, it can be said that there are no significant differences between results when considering numerical uncertainty, which was found to be small. This shows that the scatter observed in the initial study is unlikely to be the result of any differences

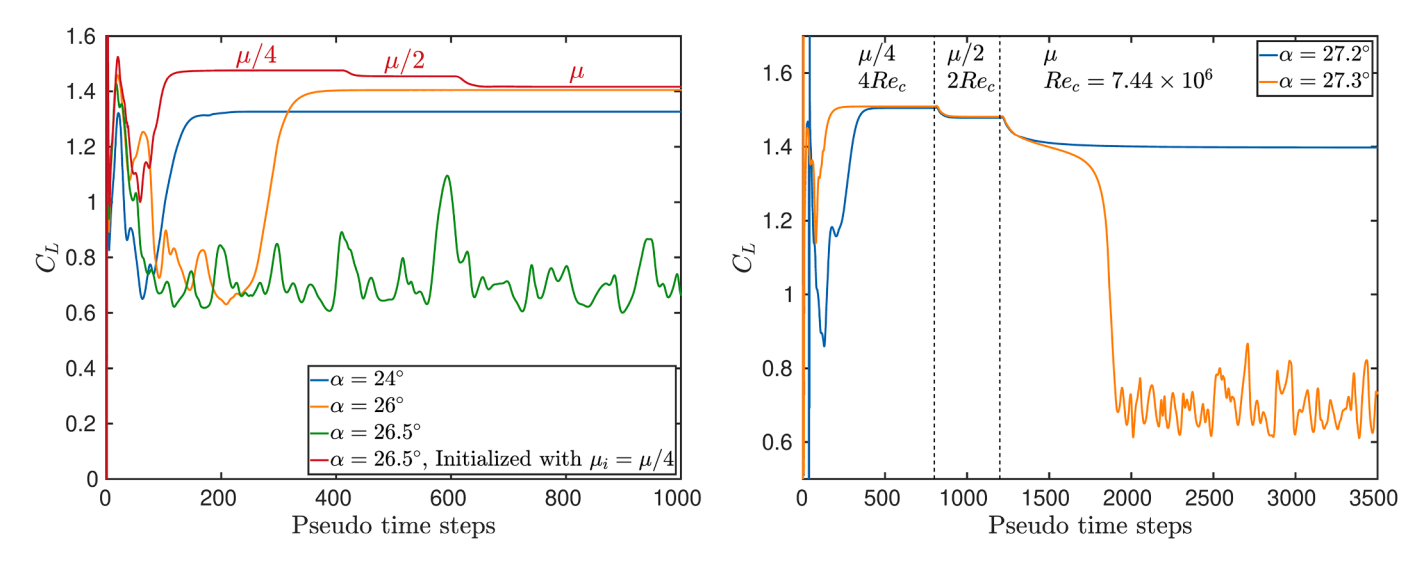


Fig. 22. Convergence of C_L for some of *DRDC*'s Ansys CFX computations with grid L10 for $Re_c = 7.44 \times 10^6$. The velocity in the entire domain was initialized to the free-stream value in all cases. For one case at 26.5° (red curve), the fluid viscosity and corresponding Reynolds number were varied as follows: $[\mu/4, Re_c = 29.8 \times 10^6]$ for the first 400 timesteps, $[\mu/2, Re_c = 14.9 \times 10^6]$ for timesteps 401 to 600, and $[\mu, Re_c = 7.44 \times 10^6]$ for timestep 601 to the end, where μ is the assumed dynamic viscosity for air used in this benchmark case. For $\alpha = 27.2^\circ$ and $\alpha = 27.3^\circ$, the viscosity was set to $\mu/4$ for the first 800 timesteps, $\mu/2$ for timesteps 801-1200, and to μ from timestep 1201 to the end.

Table 8 Finest grid and L5 grid solutions, with estimated uncertainties, for $Re_c = 7.44 \times 10^6$, $\alpha = 24^\circ$. The exponent p is given for cases where a single-term fit was used in the uncertainty analysis, otherwise the use of a two-term fit is indicated.

Submission	Finest grid for	submission		Grid L5			
(Finest Grid)	C_L	C_D	$1000C_{Mz}$	C_L	C_D	$1000C_{Mz}$	
MARIN	$1.327 \pm 0.4\%$	$0.2339 \pm 1.0\%$	$4.0 \pm 86\%$	$1.307 \pm 2.4\%$	$0.2271 \pm 4.8\%$	$-3.8 \pm 357\%$	
REFRESCO (L12)	p = 1.72	p = 1.94	p = 1.55	p = 1.94	p = 1.72	p = 1.55	
Naval Group	1.329 ± 0.4%	$0.2347 \pm 0.3\%$	$5.2 \pm 17\%$	1.323 ± 0.1%	$0.2332 \pm 1.2\%$	$3.3 \pm 101\%$	
STAR-CCM+ (L12)	two-term	p = 2	p = 1.83	two-term	p = 2	p = 1.83	
DRDC	$1.327 \pm 0.2\%$	$0.2343 \pm 1.0\%$	$4.9 \pm 55\%$	$1.320 \pm 1.0\%$	$0.2318 \pm 2.4\%$	$1.8 \pm 360\%$	
Ansys CFX (L12)	p = 2	p = 1.04	p = 1.05	p = 2	p = 1.04	p = 1.05	
CNR-INM OpenFOAM (L12) UNB Ansys Fluent (L8)	$1.331 \pm 0.7\%$	$0.2351 \pm 0.2\%$	$5.5 \pm 12\%$	$1.327 \pm 1.6\%$	$0.2338 \pm 0.9\%$	$3.8 \pm 76\%$	
	p = 1	p = 1.97	p = 1.73	p = 1	p = 1.97	p = 1.73	
	$1.327 \pm 0.4\%$	$0.2345 \pm 0.7\%$	$5.0 \pm 26\%$	$1.321 \pm 1.0\%$	$0.2334 \pm 1.8\%$	$3.5 \pm 96\%$	
	p = 2	p = 2	p = 2	p = 2	p = 2	p = 2	
QinetiQ	$1.331 \pm 0.9\%$	$0.2348 \pm 0.2\%$	$5.4 \pm 12\%$	$1.323 \pm 1.6\%$	$0.2332 \pm 1.1\%$	$3.3 \pm 100\%$	
STAR-CCM+ (L12)	p = 0.66	p = 2	p = 1.86	p = 0.66	p = 2	p = 1.86	
Chalmers	$1.329 \pm 0.4\%$	$0.2349 \pm 0.6\%$	$5.2 \pm 29\%$	$1.321 \pm 1.2\%$	$0.2327 \pm 1.8\%$	$2.8 \pm 162\%$	
STAR-CCM+ (L10)	p = 2	p = 1.54	p = 1.57	p = 2	p = 1.54	p = 1.57	
NSWCCD-p	$1.329 \pm 0.4\%$	$0.2346 \pm 0.6\%$	5.0 ± 11%	$1.324 \pm 1.0\%$	$0.2332 \pm 1.6\%$	3.6 ± 67%	
NavyFOAM (L8)	p = 2	p = 2	two-term	p = 2	p = 2	two-term	

in the underlying equations being solved by each code (e.g., slight differences in the SST turbulence versions). It is clear that the initialization and solution process are both influential in determining whether a high-lift, attached-flow or a low-lift, detached-flow solution is obtained at large angles of attack just below the critical angle for deep stall. Initialization with an inviscid method (potential flow or Euler equations), or with low viscosity, and the use of an unsteady or pseudo-transient solution method have the tendency to produce the high-lift solution in this situation. The typical approach of initializing the RANS equations with the uniform undisturbed free-stream velocity has a tendency to produce a stalled condition. The same observations and conclusion were obtained when this grid study was repeated for $\alpha = 22^\circ$ at $Re_c = 1 \times 10^6$. All solvers produced consistent results, to within discretization uncertainty, when initialized in a manner that produced the high-lift solution.

5.5. Local flow quantities

The predictions for chord-wise variation of c_p and τ_x' are shown in Fig. 21 for $\alpha=24^\circ$ at $Re_c=7.44\times10^6$. There are no noticeable differences in pressure between all the attached-flow solutions. They give a peak minimum c_p of close to -7.5. This large negative peak is an important consideration for cavitation analysis (Molland and Turnock, 2022). The NSWCCD-v results are shown as an example of a stalled solution. The peak negative c_p on the suction side is roughly half that of the attached-flow solutions, while the pressure side changes are relatively small. The agreement between attached flow solutions for τ_x is also generally good, but there are some noticeable differences for the peak value on the suction side near the leading edge. There are also two groups of solutions for the shear stress near the tip (z/b=0.9). Here, the Open-FOAM and NavyFOAM results are shifted around 10-15% higher than

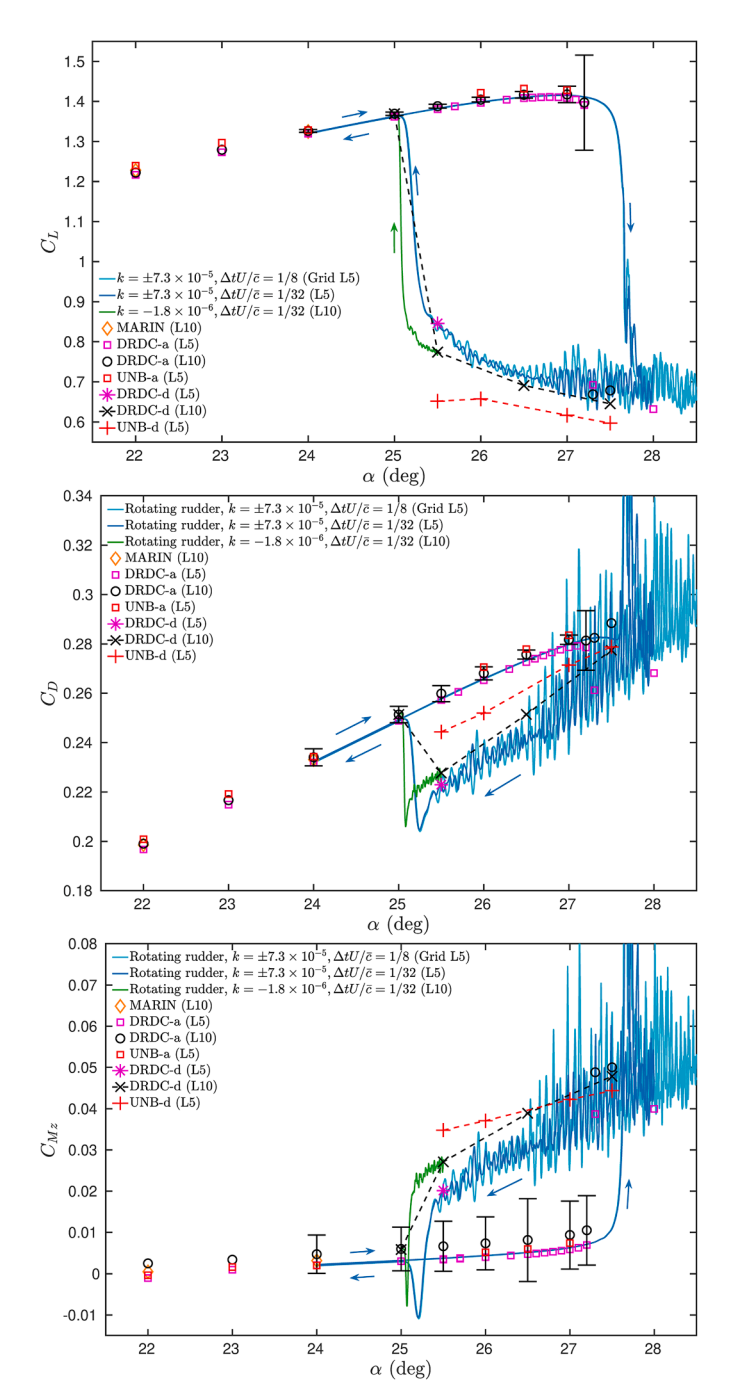


Fig. 23. Computed lift, drag, and pitching moment coefficients as a function of angle of attack, α , at $Re_c=7.44\times10^6$. Symbols: computations at static α ; solid lines: rotating rudder URANS simulations with low reduced yaw rate, $k=\dot{\alpha}\bar{c}/(2U_{\infty})$. The following flow solvers were used: Ansys CFX for the rotating rudder and *DRDC* computations, REFRESCO for the *MARIN* computations, and Ansys Fluent for the *UNB* computations. The error bars show the estimated discretization uncertainty for the *DRDC*-a results with the L10 grid. The *DRDC*-d and *UNB*-d computations were initialized with higher than nominal fluid viscosity to force a stalled flow state at lower Reynolds number before adjusting the viscosity to achieve $Re_c=7.44\times10^6$; these cases were then run with URANS and the average force over several convection times is shown.

the rest from around 40% of the chord to the trailing edge. The cause of these differences is not known, but it may be a result of slight differences in the SST model or numerical methods implemented in these solvers. However, these differences in shear stress do not result in a significant difference in the total integrated forces and moment because they are localized to a relatively small area over the rudder and there is excellent

agreement in the pressure which is the primary contributor to the total force. It is also noted that the differences in wall shear stress due to predicted flow condition (i.e., attached versus detached) are much larger than the differences between solvers for the attached-flow solution, as expected.

5.6. Static hysteresis loop evaluation

In this section, the same grids and solution procedures studied in the $\alpha=24^\circ$ verification study are used to evaluate a static hysteresis loop at larger angles-of-attack. In Section 5.6.1, we first evaluate the high lift branch of the hysteresis loop by controlling the solution to start from attached flow. Then in Section 5.6.2, we compute the low lift branch by forcing a stalled initial condition. In Section 5.6.3 we show the flow fields for both branches in the hysteresis loop. Finally, in Section 5.6.4, we confirm the static hysteresis loop using URANS computations of a slowly rotating rudder.

5.6.1. High lift branch

DRDC used the Ansys CFX solver to determine the upper branch of the hysteresis loop at $Re = 7.44 \times 10^6$ by repeating their $\alpha = 24^\circ$ calculations at larger angles of attack. It was found that free-stream initialization and the pseudo-transient method of Ansys CFX consistently produced stable high-lift solutions for $\alpha \le 26^{\circ}$, and then deep-stall, low- C_L flow at larger angles. The low-viscosity initialization method previously demonstrated by Chalmers was applied for $\alpha > 26^{\circ}$. However, it was found that initialization with the viscosity set to a quarter of the nominal value was sufficient for establishing an attached flow solution at a higher Reynolds number, as shown in Fig. 18 for $\alpha = 26.5^{\circ}$. For this case, the viscosity was then doubled at timestep 401 and held until timestep 600 to establish another steady result at $Re_c = 14.9 \times 10^6$. At timestep 601, the viscosity was again doubled to achieve the target Reynolds number of $Re_c = 7.44 \times 10^6$ and held until the end of the computation. Each time the viscosity was adjusted, there was a smooth transition to a new solution at a lower Reynolds number. This method was applied for angles of attack up to the static stall stability limit, which was determined to be $\alpha = 27.2^{\circ}$, as demonstrated in Fig. 22. At $\alpha = 27.2^{\circ}$, the solution slowly transitioned to a new stable solution when the Reynolds number was halved. The same transition is initially seen for $\alpha = 27.3^{\circ}$ but then the lift coefficient diverges from a value of 1.4 down to around 0.7. Oscillations with peak-to-peak amplitude of $\pm 14\%$ are then established in this deep-stall flow regime.

UNB also determined the static stall angle, but in this case using the Ansys Fluent solver with potential-flow initialization and a URANS method with first order discretization in time. The stability limit for attached flow was found to be 27°, in agreement with the Ansys CFX result (since a 0.5 degree increment was used for Ansys Fluent and the 27.5° computation gave a deep-stall result). The Ansys Fluent (UNB-a) and Ansys CFX (DRDC-a) force and moment predictions for the upper branch of the hysteresis loop are compared in Fig. 23, together with MARIN computations done with the L10 grid at lower angles of attack (note that the other results that are overlaid in Fig. 23 will be discussed in Sections 5.6.2 and 5.6.4). Overall, the agreement is good, considering that discretization errors are likely to have a modest effect as the Ansys Fluent computations were done with the L5 grid. The Ansys CFX results shown are for the L5 and L10 grids and the error bars were computed using the uncertainty analysis described earlier. Grids L4 to L10 were used for this uncertainty analysis, except the coarse L4 grid was excluded for $\alpha = 27^{\circ}$ and 27.2° because the high-lift solution could not be obtained for that grid at those angles.

The lift curve becomes very non-linear above $\alpha=24^\circ$ and peaks somewhere between 26.5° and 27°. Beyond that, the most consequential change due to stall is the $\approx 50\%$ drop in C_L . However, there is also a significant increase in torque about the rudder axis as C_{Mz} increases from 0.01 to 0.05. This indicates that the centre of pressure shifts towards the trailing edge with deep stall. There is very little change in

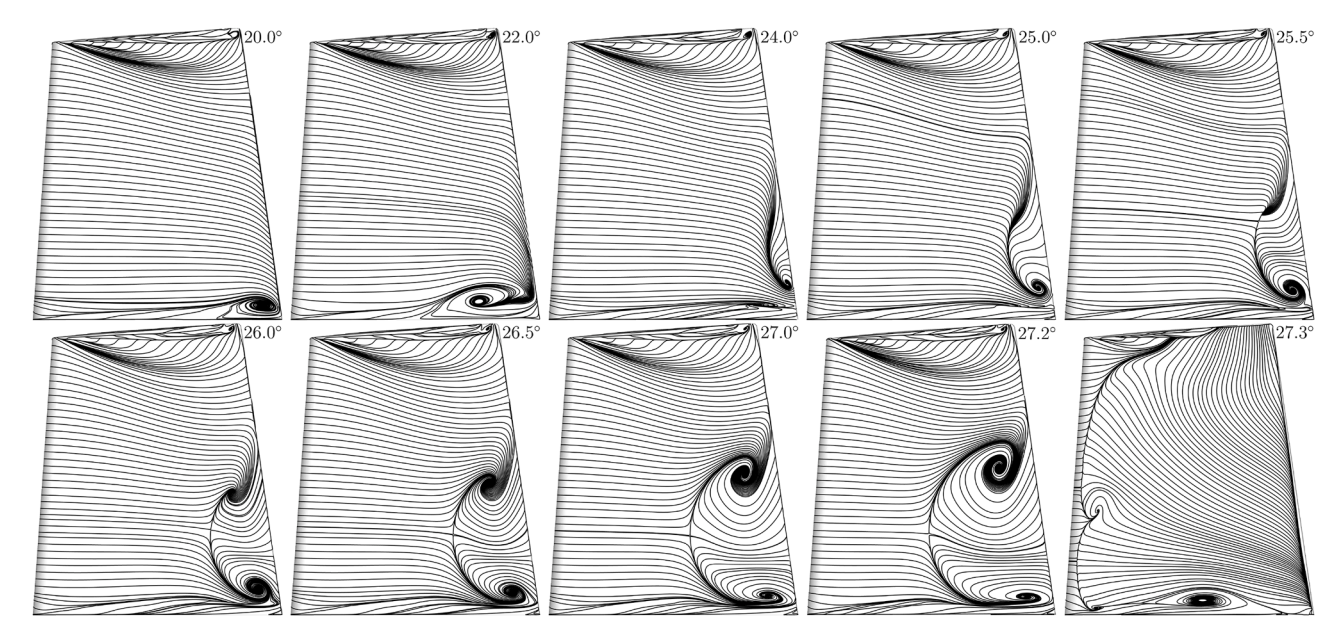


Fig. 24. DRDC-a results for the suction-side limiting streamlines, $Re_c = 7.44 \times 10^6$. The image has been mirrored so that the flow is from left to right.

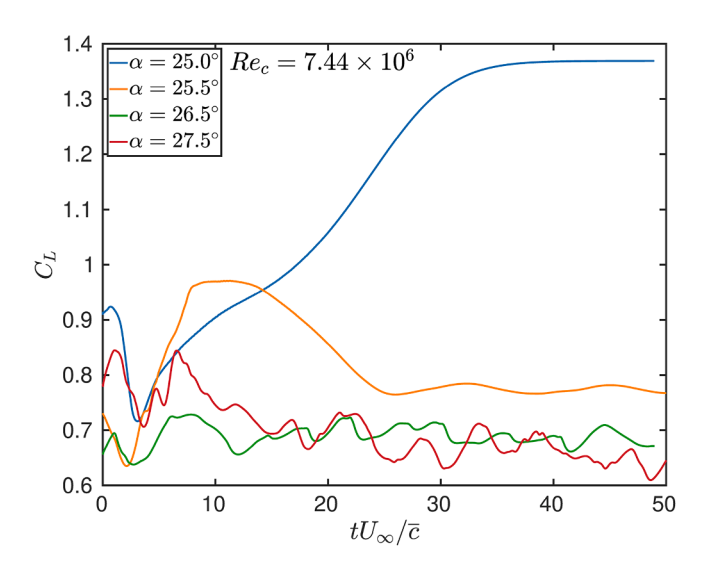


Fig. 25. Progression of C_L with non-dimensional time for Ansys CFX URANS computations with the SST-2003 turbulence model at $Re_c=7.44\times10^6$ (DRDC-d). Computations are initialized from a RANS solution with viscosity set to 2μ ($Re_c=3.72\times10^6$).

the drag coefficient before and after stall. While the drag is expected to increase due to the larger separation zone, there is a corresponding drop in the lift-induced drag and it appears that these effects approximately cancel. However, note that this is sensitive to grid refinement – the L5 grid predicts a drop in C_D of around 7% but the fine L10 grid predicts approximately no change when going from $\alpha=27.2^\circ$ to $\alpha=27.3^\circ$. It should be noted that URANS computations of the stalled flow around this angle of attack (to be discussed fully in Section 5.6.2) show that the flow is unsteady with predicted peak-to-peak oscillations on the order of 15%. Steady RANS does not converge well for this reason, and iterative errors contribute to the large difference between the L5 and L10 results.

Fig. 24 shows how the limiting streamlines on the suction side of the rudder change as the angle is increased from 20° to 27.3°, following the upper lift branch of the hysteresis loop. At 20°, there is a clear corner vortex around the intersection between the root chord and the trailing edge. This vortex is within the floor boundary layer, which is approx-

imately 0.2 m high, or $\approx 0.09\overline{c}$. This corner vortex becomes larger at $\alpha = 22^{\circ}$, being stretched primarily in the chord-wise direction with the height extending just above the boundary layer. By $\alpha = 24^{\circ}$ a small trailing edge recirculation zone has formed, which extends from around the top of the boundary layer to around mid-span. This region grows into a distinct 'owl face pattern' by around $\alpha = 25.5^{\circ}$, in which there are two nodes separated by a saddle point. As the angle of attack is increased further, the saddle point moves upstream and the upper node moves spanwise towards the tip. At $\alpha = 27.2^{\circ}$, the saddle point at the leading edge of the owl face pattern has moved up to approximately mid-chord and the upper node is around mid-span. This flow pattern is not stable in the numerical model beyond the critical angle of $\alpha = 27.2^{\circ}$ and a very different shear pattern with leading-edge stall was obtained at $\alpha = 27.3^{\circ}$. This change corresponds to the large drop in the lift curve. Note that this static analysis does not capture a dynamic process, with intermediate flow states, that occurs as the angle is increased beyond the critical angle (from 27.2° to 27.3°). An analysis of stall dynamics is planned as a follow-on to this benchmark study.

5.6.2. Low lift branch

In order to evaluate the lower- C_L branch of the hysteresis loop, a deep-stall flow field was established for a given static angle by initializing with a low Reynolds number / high viscosity fluid in a process opposite of the low-viscosity initialization method described earlier. URANS computations were used because the deep-stall flow is inherently unsteady. Fig. 25 shows how the lift coefficient evolves in the Ansys CFX URANS computations, which were initialized from a detached flow field obtained with viscosity set to 2μ ($Re_c = 3.72 \times 10^6$). It was found that a deep-stall flow could be maintained in the URANS computations down to $\alpha = 25.5^{\circ}$. At $\alpha = 25^{\circ}$, the solution proceeded slowly to the high-lift solution over more than 30 convection times, a time scale similar to that indicated by Le Fouest et al. (2021). Note that this URANS computation, with second order temporal discretization, arrives at precisely the same steady solution as the steady RANS computation, suggesting that the flow is statistically steady at $\alpha = 25^{\circ}$. Similar computations were done with Ansys Fluent (UNB-d). The mean values of forces and moment were calculated over several convection times after a steady periodic solution was obtained and plotted in Fig. 23. This shows a static hysteresis loop in the approximate range of $25^{\circ} < \alpha \le 27.2^{\circ}$. Below that range, the flow attaches in URANS computations if run sufficiently long, regardless of the initialization. Above that range, only the deep-stall solution with

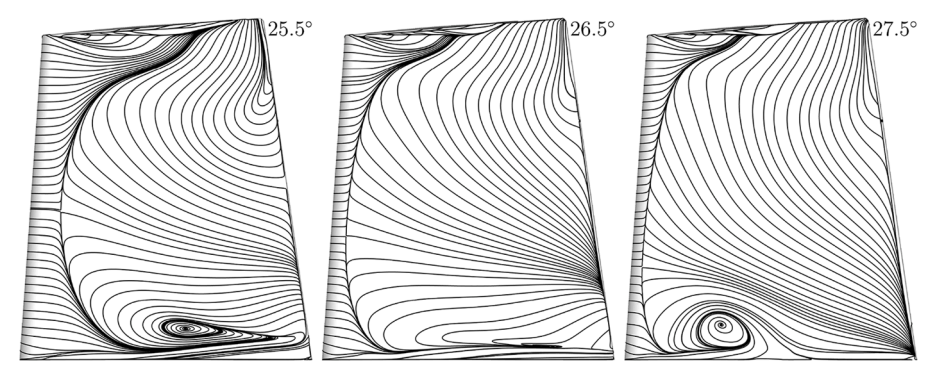


Fig. 26. DRDC-d time-averaged Ansys CFX results for the suction-side wall shear lines for $Re_c = 7.44 \times 10^6$. The image has been mirrored so that the flow is from left to right.

leading edge separation could be obtained, regardless of initialization or solver method.

Fig. 26 shows the time-averaged shear lines for *DRDC*-d results ranging from $\alpha = 25.5^{\circ}$ to 27.5° . The separation line is close to the leading edge in all cases, but it progresses further forward as the angle is increased.

5.6.3. Comparison of flow fields for upper and lower branches

Within the hysteresis range, two very different flow patterns are obtained for the two branches, as shown in Fig. 27 for $\alpha=26.5^{\circ}$. When starting from an attached-flow condition, the flow remains attached with only a small region of separated flow near the trailing edge. The horseshoe vortex generated upstream of the rudder remains strong and coherent several rudder chords downstream of the model. When starting from a detached-flow, the flow remains detached with a large region of separated flow. The Q-isosurface for an instant in the URANS solution shows periodic vortex shedding from the bottom half of the span. This shedding frequency corresponds to the oscillations in lift shown in Fig. 25.

5.6.4. Slowly rotating rudder computations

To confirm the hysteresis loop in another way, Ansys CFX computations were also run with very low reduced yaw rate, $k = \dot{\alpha} \bar{c}/(2U_{\infty})$, where $\dot{\alpha}$ is the rate of change in angle-of-attack in radians/s. The resulting force and moment coefficients are overlaid on the static results in Fig. 23. Two computations were done with grid L5 with a factor of 4 difference in timestep size. They both start at $\alpha = 24^{\circ}$ and first increase in angle-of-attack at a constant $k = 7.27 \times 10^{-5}$, which is equivalent to 1 degree of rotation every 120 convective times (defined as \bar{c}/U_{∞}). The rotation direction is reversed at $\alpha = 30^{\circ}$ for the simulation with larger timestep and at $\alpha = 28^{\circ}$ for the other. Both simulations return to $\alpha = 24^{\circ}$ with $k = -7.27 \times 10^{-5}$. These slow dynamic simulations produce a hysteresis loop that is in agreement with the static computations, with only a small delay in the stall angle for increasing α . Following Le Fouest et al. (2021), the stall angle in the dynamic case is taken to be the angle at which the lift drops by 4% of the total lift drop during stall. Based on this definition, stall occurs at $\alpha = 27.47^{\circ}$ in the dynamic case, which is 0.27° later than that predicted by the static computations. This is equivalent to a delay of 32 convective times for this rotation rate, in agreement with the experimental results of Le Fouest et al. (2021). After deep stall occurs, the rudder has to be rotated back to around $\alpha = 25^{\circ}$ before the flow re-attaches and the lift re-joins the upper branch of the hysteresis loop. Below $\alpha = 25^{\circ}$, the results for increasing and decreasing alpha are overlaid, indicating that dynamic effects are negligible below the hysteresis loop at this slow rotation rate. This indicates that the deep stall results for static computations at $\alpha = 24^{\circ}$ observed in Section 5.3 are not valid solutions. This is further confirmed with a dynamic simulation with the fine L10 grid, which starts from the stalled DRDC-d computation at $\alpha = 25.5^{\circ}$ and rotates at an even lower reduced yaw rate of $k = -1.8 \times 10^{-6}$. As indicated by Fig. 23, the flow in this case also re-attaches by $\alpha = 25^{\circ}$.

6. Summary and Conclusion

A new generic marine rudder geometry, the AVT-392 rudder, was defined for benchmark CFD and experimental studies with a focus on rudder stall. It shares several overall features with the BB2 submarine's aft control surfaces (ACSs), such as a NACA0016 profile and trailing edge rounding, and it has approximately the same aspect ratio and taper. However, the sweep and tip inclination angles for the AVT-392 rudder were selected to approximate the flow incidence seen by the hull-mounted BB2 ACS when mounted to the wind tunnel floor. While designed to be relevant for submarine ACSs, the AVT-392's low aspect ratio and taper are expected to make it relevant for a wide range of marine vehicle control surfaces.

A numerical benchmark was defined to study RANS/URANS predictions of the AVT-392 rudder stall characteristics, with the aim of understanding and resolving the issue of RANS computations giving inconsistent predictions for the BB2 ACSs stall in a previous study. Consistent RANS/URANS predictions are needed for efficiently and reliably predicting marine vehicle manoeuvring loads in practical applications. Reynolds numbers of $Re_c = 1 \times 10^6$ and $Re_c = 7.44 \times 10^6$ were selected for the study because they are the bounds for the achievable Reynolds numbers in large-scale wind tunnel experiments that are currently being planned. The larger Reynolds number is also within the full-scale range of operation for a conventional submarine. Initial predictions were done independently by seven organizations and five flow solvers using typical grids and methods to see if the inconsistencies for the BB2 ACS stall predictions would be replicated with the AVT-392 rudder. Indeed, this was found to be the case, indicating that the issue persists in the absence of a hullform. There was a 4-5 degree spread in the initial predictions for stall angle even when using the same nominal SST turbulence model. This initial (Phase 1) study was thus deemed a success because it showed we could study the issue with a simpler test case (isolated rudder instead of a fully appended submarine).

A verification study with a set of six geometrically-similar structured grids and the SST turbulence model was then undertaken at $\alpha=24^\circ$ to understand this issue. We found that two solutions could be obtained for a range of large angles of attack near stall, depending on the initialization and solution strategies. Initialization with potential flow tended to produce high-lift attached-flow solutions with small trailing edge separated flow regions (light stall), while initialization using the uniform free-stream velocity tended to produce low-lift solutions with massive separation zones, characteristic of deep-stall. The high-lift solutions could also be obtained by initializing with uniform flow but with the viscosity set temporarily lower to first establish an attached flow at higher Reynolds number; when the viscosity was stepped to the true value to achieve the target Reynolds number, the flow remained at-

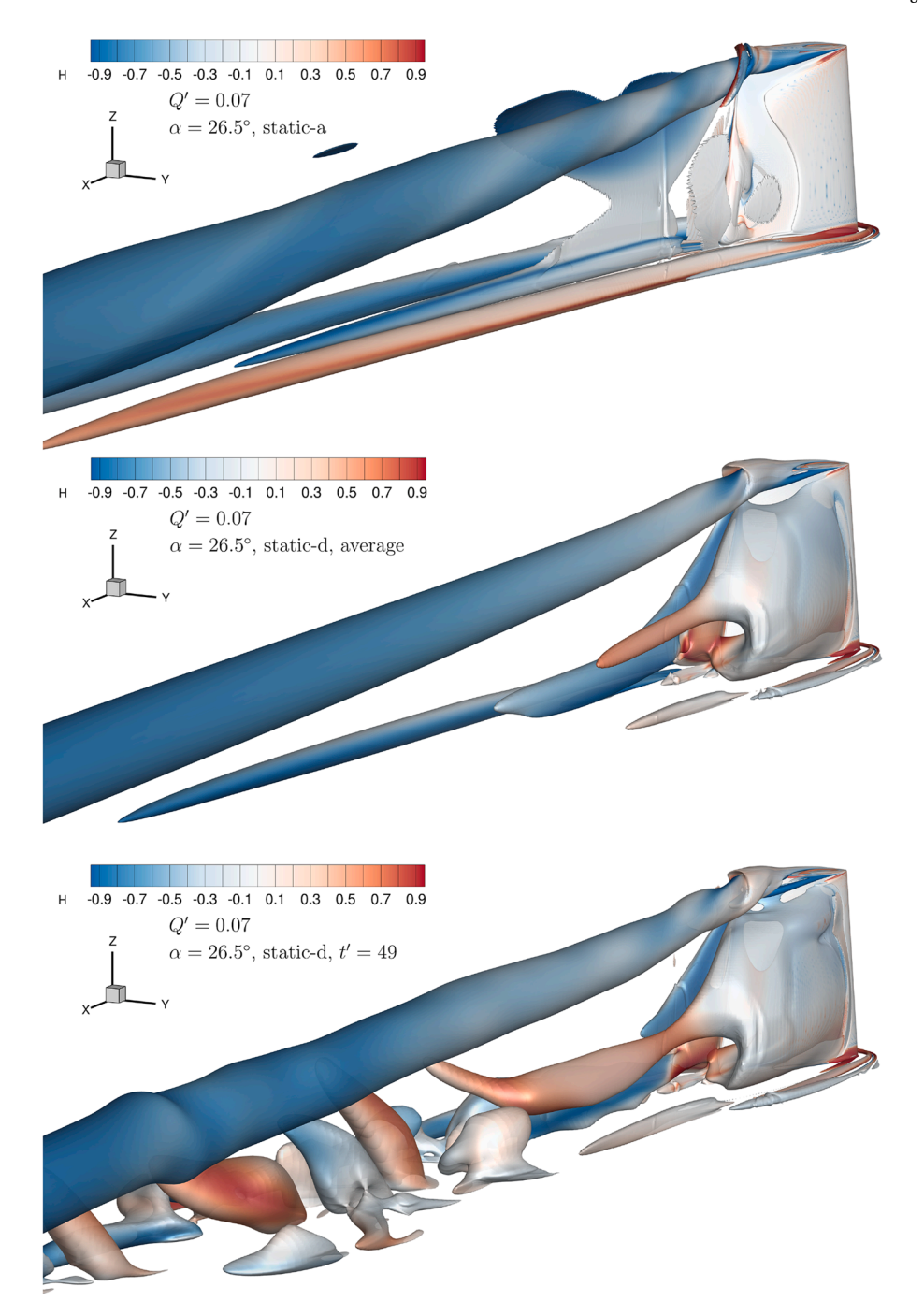


Fig. 27. Ansys CFX predictions (grid L10) of Q-criterion isosurfaces coloured by normalized helicity for $\alpha=26.5^\circ$, $Re_c=7.44\times10^6$. Top: DRDC-a RANS; middle: time-averaged DRDC-d URANS; bottom: DRDC-d URANS at $t'=tV_\infty/\overline{c}=49$.

tached. Likewise, the flow remained attached when initializing using an attached flow solution from a different grid refinement. Pseudotransient methods, either within a steady RANS method or a URANS method with first order temporal discretization and large timestep, also tended to proceed to the high-lift solution up to higher angles of attack than other steady methods. This dependence on solution strategy may explain the large scatter observed in RANS predictions of the BB2 undergoing a steady turn (NATO AVT-301 Task Group, 2022), but this should be confirmed by revisiting that problem using the lessons learned from the present study.

The verification study was then extended to larger α and it revealed a hysteresis loop that has a high lift/light stall branch and a low lift/deep stall branch, which replicates known physical behaviour. This loop is

confirmed with URANS computations of the rudder rotating slowly with increasing and decreasing angle of attack. This partially explains the inconsistencies – which solution is obtained depends on the computational starting condition and procedure. However, below the hysteresis loop, where there should only be an attached flow solution, we observe that steady RANS can produce an incorrect stalled flow. We believe this to be a result of poor iterative convergence, and it shows the danger of using steady RANS for predictions at high angles of attack close to static stall.

From this study, we have arrived at the following conclusions and recommendations:

 CFD practitioners, and those using static data for manoeuvring models, should be aware that marine rudders can exhibit a physical flow

hysteresis effect which causes two very different flows and lift coefficients over a range of angle of attack. Based on URANS simulations with slow rudder rotation, and carefully-conducted steady RANS and URANS computations at static angles, the $k-\omega$ SST model predicts this static hysteresis range to be 25° < $\alpha \leq 27.2^{\circ}$ for the new AVT-392 generic rudder benchmark case at $Re_c = 7.44 \times 10^6$. In this range, statistically-steady flow is observed for the high-lift branch. Statistically-unsteady flow, with approximately half of the lift coefficient, is computed with URANS for the lower branch.

- Due to the statistically-unsteady nature of stalled flow, steady RANS predictions are problematic for predicting rudder stall and can yield very different results for stall angle which depend on initialization and solution procedure. In this study, we found that steady RANS could produce an incorrect deep stall numerical result that is at least 1° below the start of the hysteresis loop, which is 3.2° below the critical stall angle at the end of the hysteresis loop. A steady RANS solution of stalled flow should not be accepted, or should be viewed with extreme scepticism. We recommend switching to unsteady RANS in this case. We observed in this study that URANS was effective for taking an incorrect deep-stall RANS result to a well-converged attached flow state at $\alpha = 24^{\circ}$.
- Model-scale RANS computations can significantly under-predict the stall angle for full-scale conditions. This is due to a combination of a Reynolds-number sensitivity and the previously-noted numerical issue. The earliest critical stall angle predicted at $Re_c = 1 \times 10^6$ in Phase 1 of this study was 18° , which is 9° below the critical stall angle determined for $Re_c = 7.44 \times 10^6$. This highlights the importance of carefully running computations at full-scale conditions and the need for high-Reynolds-number experiments for validation.
- While steady RANS solutions may be appropriate for the upper branch of the hysteresis loop, they are difficult to obtain unless care is taken in the numerical procedure. We found that the following methods help arrive at the upper branch: initialization with potential flow, initialization with low fluid viscosity (high Reynolds number), and the use of pseudo transient or URANS. Initialization with the free-stream, a common practice, tends to gravitate to the stalled condition
- URANS of a slowly rotating rudder can also be effective for evaluating the full hysteresis loop. However, we note that this is expensive for obtaining the static limit due to the very long timescales for stall. Our URANS simulations confirm the recommendation of Le Fouest et al. (2021) that a reduced rotation rate of $k = 1 \times 10^{-4}$ or less is required to accurately approximate static conditions. This requires many timesteps if a reasonable timestep/Courant number is to be used
- The long timescales for static stall also highlight an important point: static stall conditions are likely never relevant for real marine vehicle operation. This motivates further study on dynamic effects at realistic rates of change in angle of attack. It also highlights a potential deficiency of quasi-steady manoeuvring models if they are applied in situations where the static stall angle is exceeded.
- The method of Eça and Hoekstra (2014) was found to be useful for estimating discretization uncertainty and evaluating the consistency in solution between flow solvers. When well-converged solutions were obtained, all six flow solvers produced the same solution for lift, drag, and yawing moment for $\alpha=24^{\circ}$ at $Re_c=7.44\times10^{6}$, to within small estimated uncertainty bounds. The L5 refinement level presented in this paper was found to give reasonable agreement with much finer grids for this study. However, discretization errors are case- and solver-specific and a discretization uncertainty analysis must be performed for any given application for reliable results.
- This study deals exclusively with solution verification, with the focus
 on achieving consistent and repeatable RANS predictions for marine
 rudder stall. This is an important precursor to the assessment of the

physical accuracy of these methods using experiments, which is recommended as a follow-on to this study.

CRediT authorship contribution statement

Mark Bettle: Writing - review & editing, Writing - original draft, Visualization, Validation, Supervision, Software, Resources, Project administration, Methodology, Investigation, Funding acquisition, Formal analysis, Data curation, Conceptualization; Luc Bordier: Writing - review & editing, Writing - original draft, Visualization, Validation, Supervision, Software, Resources, Project administration, Methodology, Investigation, Funding acquisition, Formal analysis, Data curation, Conceptualization; Myriam Slama: Writing - review & editing, Writing original draft, Visualization, Validation, Software, Methodology, Investigation, Formal analysis, Data curation, Conceptualization; Emmanuel François: Writing - review & editing, Writing - original draft, Visualization, Validation, Software, Methodology, Investigation, Formal analysis, Data curation; Serge Toxopeus: Writing – review & editing, Writing - original draft, Visualization, Validation, Software, Resources, Project administration, Methodology, Investigation, Funding acquisition, Formal analysis, Data curation, Conceptualization; Craig Marshall: Writing - review & editing, Writing - original draft, Visualization, Validation, Software, Methodology, Investigation, Formal analysis, Data curation, Conceptualization; Richard Pattenden: Writing - review & editing, Writing - original draft, Visualization, Validation, Software, Resources, Methodology, Investigation, Formal analysis, Data curation, Conceptualization; Riccardo Broglia: Writing - review & editing, Writing original draft, Visualization, Validation, Software, Resources, Methodology, Investigation, Formal analysis, Data curation, Conceptualization; Shawn Aram: Writing - review & editing, Writing - original draft, Visualization, Validation, Software, Resources, Methodology, Investigation, Formal analysis, Data curation, Conceptualization; Abel Vargas: Writing - review & editing, Writing - original draft, Visualization, Validation, Software, Methodology, Investigation, Formal analysis, Data curation, Conceptualization; Rui Lopes: Writing - review & editing, Writing - original draft, Visualization, Validation, Software, Methodology, Investigation, Formal analysis, Data curation, Conceptualization; Magnus Vartdal: Writing - review & editing, Writing - original draft, Validation, Methodology, Investigation, Conceptualization; Tom Keith: Writing - review & editing, Writing - original draft, Visualization, Validation, Software, Resources, Methodology, Investigation, Formal analysis, Data curation, Conceptualization; Carl Janmark: Writing - review & editing, Writing - original draft, Visualization, Validation, Software, Resources, Methodology, Investigation, Formal analysis, Data curation, Conceptualization; Tiger Jeans: Writing - review & editing, Supervision, Resources, Methodology, Funding acquisition, Conceptualization; Andrew Gerber: Writing - review & editing, Supervision, Resources, Methodology, Funding acquisition, Conceptualization; Rickard Bensow: Writing - review & editing, Writing - original draft, Supervision, Resources, Methodology, Funding acquisition, Conceptualization; Toby Peacock: Writing - review & editing, Resources, Methodology, Data curation, Conceptualization.

Declaration of competing interest

The authors declare that they have no known competing financial interests or personal relationships that could have appeared to influence the work reported in this paper.

Acknowledgements

The first author would like thank Siddharth Raval for contributing to the *UNB* computations for the Phase 1 study, and Professor Luís Eça for helpful discussions on the discretization uncertainty analysis. Chalmers' computations were enabled by resources provided by Chalmers e-Commons at Chalmers and partly funded by the Swedish

Transport Administration and Kongsberg Maritime AB. The research by MARIN is partly funded by the Dutch Ministry of Economic Affairs and by the Dutch Materiel and IT Command (COMMIT) under programme M2429. *UNB*'s contribution was partially funded by the Natural Sciences and Engineering Research Council of Canada (NSERC) through an NSERC Alliance grant.

References

- Ansys, Inc., 2022. Ansys CFX-Solver Theory Guide, Release 2022R2. Canonsburg, PA. Aram, S., Kim, S.E., 2017. A numerical study of added resistance, speed loss and added power of a surface ship in regular head waves using coupled URANS and rigid-body
- power of a surface ship in regular head waves using coupled URANS and rigid-body motion equations. In: VII International Conference on Computational Methods in Marine Engineering (MARINE 2017). Nantes, France, pp. 960–974.
- Aram, S., Shan, H., Jiang, J., Atsavapranee, P., 2022. Numerical analysis of natural boundary layer transition and trip effect on inclined spheroid. In: AIAA SciTech Forum. San Diego, California, USA. https://doi.org/10.2514/6.2022-0047
- Bettle, M.C., 2014. Validating design methods for sizing submarine tailfins. In: RINA (Ed.), Warship: Naval Submarines & UUV's.
- Bettle, M.C., 2020. Development of computational fluid dynamics meshes for the BB2 generic submarine: Evaluation of discretization uncertainty in model-scale hydrodynamic forces for straight-ahead flight. Technical Report DRDC-RDDC-2020-R066. Defence Research and Development Canada.
- Broeren, A.P., Bragg, M.B., 2001. Spanwise variation in the unsteady stalling flowfields of two-dimensional airfoil models. AIAA Journal 39 (9), 1641–1651. https://doi.org/10.2514/2.1501
- Busquet, D., Marquet, O., Richez, F., Juniper, M., Sipp, D., 2021. Bifurcation scenario for a two-dimensional static airfoil exhibiting trailing edge stall. Journal of Fluid Mechanics 928, A3. https://doi.org/10.1017/jfm.2021.767
- Chen, X., Yao, J., 2024. RANS analysis of manoeuvring hydrodynamic performance for a submarine in six degree of freedom motion. Ocean Engineering 294, 116781. https://www.sciencedirect.com/science/article/pii/S0029801824001185. https://doi.org/10.1016/j.oceaneng.2024.116781
- Eça, L., Hoekstra, M., 2014. A procedure for the estimation of the numerical uncertainty of CFD calculations based on grid refinement studies. Journal of Computational Physics 262, 104–130. https://doi.org/10.1016/j.jcp.2014.01.006
- Eça, L., Klaij, C.M., Vaz, G., Hoekstra, M., Pereira, F.S., 2016. On code verification of RANS solvers. Journal of Computational Physics 310, 418–439. https://doi.org/10.1016/j. jcp.2016.01.002
- Eça, L., Toxopeus, S.L., Kerkvliet, M., April 2023. Procedures for the estimation of numerical uncertainties in the simulation of steady and unsteady flows. Technical Report Tech. Report M-8. IST.
- Eça, L., Vaz, G., Hoekstra, M., 2010. Code verification, solution verification and validation in RANS solvers. In: 29th International Conference on Ocean, Offshore and Arctic Engineering: Volume 6, pp. 597–605. https://asmedigitalcollection.asme.org/OMAE/proceedings-pdf/OMAE2010/49149/597/4593149/597_1.pdf. https://doi.org/10.1115/OMAE2010-20338
- ElAwad, Y.A., ElJack, E.M., 2019. Numerical investigation of the low-frequency flow oscillation over a NACA-0012 aerofoil at the inception of stall. International Journal of Micro Air Vehicles 11, 1756829319833687. https://doi.org/10.1177/ 1756829319833687
- Gertler, M., Hagen, G.R., 1967. Standard equations of motion for submarine simulation. Technical Report 2510. David Taylor Naval Ship R & D Center.
- He, K., Pan, Z., Zhao, W., Wang, J., Wan, D., 2024. Overview of research progress on numerical simulation methods for turbulent flows around underwater vehicles. Journal of Marine Science and Application 23, 1–22. https://doi.org/10.1007/ s11804.024.0043.29
- Hristov, G., Ansell, P.J., 2018. Poststall hysteresis and flowfield unsteadiness on a NACA 0012 airfoil. AIAA Journal 56 (7), 2528–2539. https://doi.org/10.2514/1.J056774
- Hunt, J.C.R., Wray, A.A., Moin, P., 1998. Eddies, stream, and convergence zones in turbulent flows. Technical Report CTR-S88. Center for Turbulence Research Report.
- Joubert, P.N., 2006. Some aspects of submarine design part 2: Shape of a submarine 2026. Technical Report DSTO-TR-2898. Defence Science and Technology Organisation.
- Kamenetskiy, D.S., Bussoletti, J.E., Hilmes, C.L., Venkatakrishnan, V., Wigton, L.B., Johnson, F.T., 2014. Numerical evidence of multiple solutions for the Reynolds-averaged Navier-Stokes equations. AIAA Journal 52 (8), 1686–1698. https://doi.org/10.2514/1.1052676
- Kim, D.-H., Kim, Y., Baek, H.-M., Choi, Y.-M., Kim, Y.J., Park, H., Yoon, H.K., Shin, J.-H., Lee, J., Chae, E.J., Shin, Y.-h., Kim, E.S., 2023. Experimental study of the hydrodynamic maneuvering coefficients for a BB2 generic submarine using the planar motion mechanism. Ocean Engineering 271, 113428. https://doi.org/10.1016/j.oceaneng.2022.113428
- Kim, S.E., Brewton, S., 2008. A multiphase approach to turbulent cavitating flows. In: 27th Symposium on Naval Hydrodynamics. Seoul, South Korea.
- Kim, S.-E., Rhee, B.J., Miller, R.W., 2013. Anatomy of turbulent flow around DARPA SUB-OFF body in a turning maneuver using high-fidelity RANS computations. International Shipbuilding Progress 60 (1), 207–231. https://doi.org/10.3233/ISP-130100
- Kim, S.-E., Schroeder, S., Jasak, H., 2010. A multiphase CFD framework for predicting performance of marine propulsors. In: 30th International Symposium on Transport Phenomena and Dynamics of Rotating Machinery. Honolulu, Hawaii, USA.
- Kim, S.-E., Shan, H., Miller, R., Rhee, B., Vargas, A., Aram, S., Gorski, J., 2017. A scalable and extensible computational fluid dynamics software framework for ship hydrody-

- Klaij, C.M., Vuik, C., 2013. SIMPLE-type preconditioners for cell-centered, colocated finite volume discretization of incompressible Reynolds-averaged Navier-Stokes equations. International Journal for Numerical Methods in Fluids 71 (7), 830–849. https://doi. org/10.1002/fld.3686
- Korkmaz, K., Kim, K., Liefvendahl, M., Werner, S., 2023. A Validation Study of Full-Scale CFD Simulation for Sea Trial Performance Prediction of Ships. In: 10th Conference on Computational Methods in Marine Engineering (Marine 2023). Madrid, Spain. https://doi.org/10.23967/marine.2023.124
- Le Fouest, S., Deparday, J., Mulleners, K., 2021. The dynamics and timescales of static stall.

 Journal of Fluids and Structures 104, 103304. https://doi.org/10.1016/j.jfluidstructs.
 2021 103304
- Lee, S.-K., Jones, M.B., Quick, H., 2023. Loads and hull-pressure measurements on a generic submarine in different stages of model build-up. Ocean Engineering 271, 113677. https://doi.org/10.1016/j.oceaneng.2023.113677
- Lee, S.-K., Manovski, P., Jones, M.B., 2024. Assessing junction boundary layer and wake flow of a benchmark submarine model with tripped appendages. Applied Ocean Research 149, 104041. https://doi.org/10.1016/j.apor.2024.104041
- Liefvendahl, M., Fureby, C., 2017. Grid requirements for LES of ship hydrodynamics in model and full scale. Ocean Engineering 143, 259–268. https://doi.org/10.1016/j. oceaneng.2017.07.055
- Lopes, R., Eslamdoost, A., Johansson, R., RoyChoudhury, S., Bensow, R.E., Hogström, P., Ponkratov, D., 2025. Resistance prediction using CFD at model- and full-scale and comparison with measurements. Ocean Engineering 321 (June 2024). https://doi.org/10.1016/j.oceaneng.2025.120367
- Majumdar, S., 1988. Role of underrelaxation in momentum interpolation for calculation of flow with nonstaggered grids. Numerical Heat Transfer 13. https://doi.org/10.1080/ 10407788808913607
- Maritime Research Institute Netherlands, 2025. Verification tools. https://www.marin.nl/en/research/free-resources/verification-and-validation/verification-tools. Accessed: 2025-05-28.
- Menter, F.R., 1994. Two-equation eddy-viscosity turbulence models for engineering applications. AIAA Journal 32 (8), 1598–1605. https://doi.org/10.2514/3.12149
- Menter, F.R., Kuntz, M., Langtry, R., 2003. Ten years of industrial experience with the SST turbulence model. Turbulence, Heat and Mass Transfer 4.
- Miller, T.F., Schmidt, F.W., 1988. Use of a pressure-weighted interpolation method for the solution of the incompressible Navier-Stokes equations on a nonstaggered grid system. Numerical Heat Transfer 14 (2), 213–233. https://doi.org/10.1080/ 10407788808913641
- Molland, A.F., Turnock, S.R., 2022. Marine Rudders, Hydrofoils and Control Surfaces: Principles, Data, Design and Applications. Butterworth-Heinemann.
- NASA Langley Research Center, 2025. Turbulence Modeling Resource: The Menter Shear Stress Transport Turbulence Model. https://turbmodels.larc.nasa.gov/sst.html. Accessed: 2025-05-28.
- NATO AVT-301 Task Group, 2022. Flowfield prediction for manoeuvring underwater vehicles. NATO TR-AVT-301 Report.
- Orych, M., Werner, S., Larsson, L., 2021. Validation of full-scale delivered power CFD simulations. Ocean Engineering 238, 109654. https://doi.org/10.1016/j.oceaneng.2021.
- Overpelt, B., Nienhuis, B., Anderson, B., 2015. Free running manoeuvring model tests on a modern generic SSK class submarine (BB2). In: MARIN (Ed.), Pacific International Maritime Conference.
- Pereira, F.S., Eça, L., Vaz, G., 2017. Verification and validation exercises for the flow around the KVLCC2 tanker at model and full-scale Reynolds numbers. Ocean Engineering 129, 133–148. https://doi.org/10.1016/j.oceaneng.2016.11.005
- Renilson, M., 2018. Submarine Hydrodynamics. Springer Cham. https://doi.org/10.1007/978-3-319-79057-2
- Rhie, C.M., Chow, W.L., 1983. A numerical study of the turbulent flow past an isolated airfoil with trailing edge separation. AIAA Journal 21. https://doi.org/10.2514/3.8284
- Richez, F., Leguille, M., Marquet, O., et al., 2016. Selective frequency damping method for steady RANS solutions of turbulent separated flows around an airfoil at stall. Computers & Fluids 132, 51–61. https://doi.org/10.1016/j.compfluid.2016.03.027
- Rocca, A., Cianferra, M., Broglia, R., Armenio, V., 2022. Computational hydroacoustic analysis of the BB2 submarine using the advective Ffowcs Williams and Hawkings equation with wall-modeled LES. Applied Ocean Research 129, 103360. https://doi. org/10.1016/j.apor.2022.103360
- Rumsey, C.L., 2007. Apparent transition behavior of widely-used turbulence models. International Journal of Heat and Fluid Flow 28 (6), 1460–1471. https://doi.org/10.1016/j.ijheatfluidflow.2007.04.003
- Sarras, K., Marquet, O., 2024. Competition between 2D and 3D aerodynamic stall modes in transitional flows around a NACA0012 airfoil at Re = 90000. In: 9th European Congress on Computational Methods in Applied Sciences and Engineering.
- Sereez, M., Abramov, N., Goman, M., 2024. CFD simulations and phenomenological modelling of aerodynamic stall hysteresis of NACA 0018 wing. Aerospace 11 (5). https://www.mdpi.com/2226-4310/11/5/354. https://doi.org/10.3390/aerospace11050354
- Shih, T.-H., Liou, W.W., Shabbir, A., Yang, Z., Zhu, J., 1994. A new k-epsilon eddy viscosity model for high Reynolds number turbulent flows: Model development and validation. Technical Report 106721. NASA Lewis Research Center.
- Simonet, T., Ducoin, A., Rakotomalala, Q., Riou, M., Yvin, C., 2024. Experimental study on dynamic stall of rigid and flexible hydrofoils in towing tank. Ocean Engineering 314, 119621. https://doi.org/10.1016/j.oceaneng.2024.119621
- Terziev, M., Tezdogan, T., Incecik, A., 2022. Scale effects and full-scale ship hydrodynamics: A review. Ocean Engineering 245, 110496. https://doi.org/10.1016/j.oceaneng. 2021.110496

- Thompson, N., 2017. Joubert BB2 rotating arm experiments. QinetiQ Internal Report.
- Toxopeus, S.L., Kerkvliet, M., Vogels, R., Quadvlieg, F. H.H.A., Nienhuis, B., 2022. Submarine hydrodynamics for off-design conditions. Journal of Ocean Engineering and Marine Energy 8, 499–511. https://doi.org/10.1007/s40722-022-00261-y
 Vargas, A., Shan, H., Holm, E., 2019. Using CFD to predict ship resistance due to bio-
- Vargas, A., Shan, H., Holm, E., 2019. Using CFD to predict ship resistance due to biofouling, and plan hull maintenance. In: 4th Hull Performance and Insight Conference. Gubbio, Italy.
- Vaz, G., Jaouen, F.A.P., Hoekstra, M., 2009. Free-surface viscous flow computations. Validation of URANS code FresCo. In: 28th International Conference on Ocean, Offshore and Arctic Engineering (OMAE). Honolulu, Hawaii. https://doi.org/10.1115/OMAE2009-79398
- Weller, H.G., Tabor, G., Jasak, H., Fureby, C., 1998. A tensorial approach to computational continuum mechanics using object-oriented techniques. Computer in Physics 12 (6), 620–631. https://doi.org/10.1063/1.168744
- Whicker, L.F., Fehlner, L.F., 1958. Free-stream characteristics of a family of low-aspectratio, all-movable control surfaces for application to ship design. Technical Report Report 933. David Taylor Model Basin.
- Yao, J., Liu, Z., Song, X., Su, Y., 2021. Ship manoeuvring prediction with hydrodynamic derivatives from RANS: Development and application. Ocean Engineering 231, 109036. https://www.sciencedirect.com/science/article/pii/S0029801821004716. https://doi.org/10.1016/j.oceaneng.2021.109036
- Zaman, K.B.M.Q., McKinzie, D.J., Rumsey, C.L., 1989. A natural low-frequency oscillation of the flow over an airfoil near stalling conditions. Journal of Fluid Mechanics 202, 403–442. https://doi.org/10.1017/S0022112089001230